NASA Contractor Report 182032

A MULTIBLOCK/MULTIZONE CODE (PAB 3D-v2) FOR THE THREE-DIMENSIONAL NAVIER-STOKES EQUATIONS: PRELIMINARY APPLICATIONS

Khaled S. Abdol-Hamid

ANALYTICAL SERVICES AND MATERIALS, INC.
Hampton, Virginia

(NASA-CR-182032) A MULTIBLOCK/MULTIZONE   N90-21745
CODE (PAB 3D-v2) FOR THE THREE-DIMENSIONAL
NAVIER-STOKES EQUATIONS: PRELIMINARY
APPLICATIONS Final Report (Analytical   Unclas
Services and Materials) 80 p   CSCL 01A G3/02 0280235

NASA

National Aeronautics and
Space Administration

Langley Research Center
Hampton, Virginia 23665

Table of Contents

List of Figures

Nomenclature

a_1	Johnson-King modeling constant
A^+, A_1^+	Van Driest damping constants
A,B,C_1,C_2	Goldberg turbulence model constants
C_{cp}	Cebeci constant
C_D	turbulence diffusion constant
C_{kleb}	Klebanoff's intermittency function
C_p	pressure coefficient
D	jet diameter
e	total energy
E,F,G	flux vector in x,y and z direction respectively
$\hat{E},\hat{F},\hat{G}$	flux vector in ξ,η and ζ directions
$\hat{F}_v,\hat{G}_v$	viscous flux vector in η and ζ directions
ℓ	mixing length scale
L	afterbody model length
L_m	dissipation length scale
P	pressure
P_a	free stream pressure
P_j	jet centerline pressure
PNS	parabolized Navier Stokes
$\hat{Q}$	conservative variables
R,S,T	directed surface area of cell face in ξ,η and ζ directions
r_e	jet equivalent radius
r_j	jet radius
SMS	space marching scheme
u,v,w	velocity component in x,y,z directions
x	coordinate in streamwise direction

y	horizontal coordinate
z	vertical coordinate
γ	ratio of specific heats
$\delta_\xi, \delta_\zeta, \delta_\eta$	differencing operator in ξ, ζ and η
δ	boundary layer thickness
ξ	streamwise direction
ζ	circumferential direction
η	radial direction
μ	total dynamic viscosity
μ_t	turbulent viscosity
μ_L	laminar viscosity
ρ	density
τ	turbulent Reynolds shear stress
ω	vorticity

Subscripts

c_r	edge of separation bubble
i	inner part of boundary layer
ℓ	laminar
m	values of quantity where τ is a maximum
o	outer part of boundary layer
s	edge of the separated region
t	turbulent
v	turbulent viscous sublayer region
w	wall

Abstract

This report describes the development and applications of multiblock/ multizone and adaptive grid methodologies for solving the three-dimensional simplified Navier-Stokes equations. The program was initiated in 1987 focusing on developing a three-dimensional plume code to simulate the aerodynamic characteristics of a jet, issuing from nonaxisymmetric nozzles. Previously, Abdol-Hamid et. al. introduced the single zone version of the present code (PAB3D-v1) where the parabolized and simplified Navier-Stokes equations were solved. The code was tested and compared with the experimental data for axisymmetric underexpanded and overexpanded supersonic jet flows and transonic flow around a nonaxisymmetric afterbody.

In the present report, adaptive grid and multiblock/multizone approaches are introduced and applied to external and internal flow problems. These new implementations increase the capabilities and flexibility of the PAB3D code in solving flow problems associated with complex geometry.

1. Introduction

A single block solver can be used efficiently to simulate simple aerodynamic configurations. Among various methods offered by many researchers, Abdol-Hamid [1,2,3] introduced the single block version of PAB3D code to simulate underexpanded and overexpanded supersonic jets issued from round and rectangular nozzles. Abdol-Hamid and Compton[4] used the PAB3D code to simulate external flow around a nonaxisymmetric nozzle at a Mach number of 1.2. Pao and Abdol-Hamid[5] used the single block with adaptive grid to simulate underexpanded supersonic jet flows issued from round, square, and elliptic nozzles.

As better computational methods and powerful computers are available in recent years, computational fluid dynamics (CFD) has become one of the important tools in improving aircraft design (6,7). Until recently, the use of CFD was limited to simple geometries. Future aircraft (fighter or transport) will have very complex geometries and are difficult to handle with a single zone structured grid. Either unstructured or multiblock/multizone structured grids are attractive approaches for solving viscous flow problems with complex configurations. Even though the unstructured grid is much easier to generate, it requires more computational time and memory for solving the Navier-Stokes equations per grid point. With the capability of the supercomputers of today, the multiblock/multizone approach is a flexible method which can handle very complex configurations.

The advantages in using the multiblock/multizone approach are:

1. Simple grid generation for complex configurations.
2. Flexibility to use a different CFD approach for each block:
   a. Numerical technique (space marching algorithms for supersonic flows and time-dependent algorithms for subsonic and separated flows).
   b. Different topology for each block (polar, cartesian, etc.).

1

c. Adaptive grid in regions where the dependent variables and their gradients change their strength and location.

3. Less memory as each zone is solved independently with appropriate boundary conditions.

This report describes the capabilities of an improved version of the PAB 3D-v1 code reported in references 1 to 4. This improved code, named PAB 3D-v2, includes options for three different numerical schemes to solve the simplified Navier-Stokes equations. The three schemes are: the flux-vector-splitting scheme of van Leer[8], the flux-difference-splitting scheme of Roe[9] and a modified Roe scheme (space marching scheme)[2,3]. Four different turbulence model options are also included in PAB 3D-v2. The first of the four, the Baldwin-Lomax[10] model, is a two-layer algebraic model which follows the pattern adopted by Cebeci[11] but avoids the necessity of determining the boundary layer thickness. The second, the Johnson and King model[12] as extended to three-dimensional flows by Abid[13] and Abid et. al.[14], is a two-layer hybrid eddy-viscosity Reynolds shear-stress model in which a simplified ordinary differential equation for the maximum Reynolds shear-stress is solved. The third, the Goldberg model[15] as modified by Goldberg and Chakravarthy[16], can be considered as a three-layer turbulence model where the third layer is used to simulate the separated regions of the flow. The last is the mixing length turbulence model[2] with the option of including a compressibility correction factor introduced by Cheuch[17]. Two different external and one internal flow problems are used to test the various code capabilities.

One important problem for CFD applications is the prediction of the shock-cell structure of underexpanded and overexpanded supersonic jet flows. Understanding the effect of shock-cell structure and interaction of a supersonic jet with the external stream is essential for the design of future aircraft. Also, the nozzle exit geometry plays an important role in designing fighter aircraft for maximum maneuverability over a wide range of Mach numbers[18-22]. Developing an efficient computational technique is

2

important to fully understand the flow characteristics of these nozzles. At the present time, there are few codes available to predict the aerodynamics of three-dimensional shock containing jets. Wolf et. al. developed a three-dimensional code (SCIP3D[23]) for analyzing the propulsive jet mixing problem. Anderson and Barber[24] also developed a three-dimensional Parabolized Navier-Stokes procedure for calculating the heated subsonic and supersonic jet. This code was used to simulate the jet mixing rate for axisymmetric, rectangular and splayed nozzles operated at design conditions. Abdol-Hamid[2,3,4] introduced a space marching scheme, which is based on modifying the Roe's scheme, to get an accurate solution to the simplified Navier-Stokes equations for supersonic flows with a single time sweep. This scheme was successfully used to simulate underexpanded supersonic round and square jet flow problems[2,3]. Pao and Abdol-Hamid[5] introduced a new adaptive grid for analyzing the aerodynamic of shock-containing single jets. They used this technique to simulate round, square, and elliptic jet flows. The adaptive grid is used to accurately describe the shear layer and detect and track the movement of the shock system for underexpanded supersonic jets. In the present report, adaptive grid and multiblock capabilities included in PAB 3D-v2 are utilized to simulate round, square, and elliptic supersonic jet flows.

Another group of underexpanded supersonic jet flow which involving the internal and external flow regions for a special family of jet nozzle is analyzed in this report. These examples are designed for showing the flexibility of the PAB3D-v2 code in handling mixed boundary conditions over a block interface. The nozzle configuration can be described as a circular pipe section followed by five equally spaced tabs. Each tab is simply the extension of an arc segment of the circular pipe for a certain length in the downstream direction. Each arc segment, representing the width of the tab, is 1/10 of the full circle. For this family of configurations, only two grid blocks are needed for calculations using the PAB3D-v2 code. It is estimated that at least 30 percent of computer resources are saved by such structural simplicity when compared to typical

3

multiblock codes. Results of analysis using PAB3D-v2 for these nozzles are qualitatively similar to the experimental results obtained by Wlezien et al[44] for nozzles with 1, 2, 4 and 8 tabs. In general, the results show that the tab nozzle configuration allows rapidly establishment of a pressure equilibrium between the underexpanded jet flow and the ambient free stream. The jet plume is found to have a higher spreading rate and a lower core flow Mach number as compared to a similarly underexpanded supersonic jet issuing from a circular nozzle without tabs.

Finally, PAB3D-v2 was used to predict the aerodynamics of an afterbody at transonic speed. In fighter development programs, a great amount of effort is spent in analyzing the afterbody flowfield to efficiently integrate the nozzle and airframe. For analyzing this complex flowfield, computational fluid dynamics is becoming increasingly useful. Previous applications of computational fluid dynamics to the afterbody problem include numerical techniques ranging from panel methods to Navier-Stokes solvers[25-33]. Abdol-Hamid and Compton[4] used four different numerical algorithms and three different turbulence models to solve the three-dimensional Navier-Stokes equations for supersonic flow over a nonaxisymmetric nozzle. Three of the algorithms were contained in the PAB3D-v1 and PAB3D-v2[1-5] and the other in the CFL3D code[31,34-36]. In the present report, the multiblock/multizone approach in PAB 3D-v2 is utilized to simulate the flow over this nonaxisymmetric nozzle at a Mach number of 0.8 using a coarse grid. Also, the performance of the three turbulence models using a fine grid topology in simulating supersonic flow are compared with experimental data.

2. Governing Equations

The governing equations under consideration here are the Reynolds-averaged Simplified Navier-Stokes equations obtained by neglecting all streamwise derivatives, $\partial/\partial\xi$, of the viscous terms. The resulting simplified Navier-Stokes equations are written in generalized coordinates and conservation form as

4

$$\frac{\partial \hat{Q}}{\partial t} + \frac{\partial \left(\hat{E} \right)}{\partial \xi} + \frac{\partial}{\partial \eta}\left(\hat{F} \right) + \frac{\partial}{\partial \zeta}\left(\hat{G} \right) = 0 \tag{1}$$

where,

$$\hat{Q} = \frac{Q}{J}$$

$$\hat{E} = \frac{1}{J}\left(\xi_t Q + \xi_x E + \xi_y F + \xi_z G \right)$$

$$\hat{F} = \frac{1}{J}\left(\eta_t Q + \eta_x E + \eta_y F + \eta_z G \right) - \frac{1}{J}\left(\eta_x E_v + \eta_y F_v + \eta_z G_v \right)$$

$$\hat{G} = \frac{1}{J}\left(\zeta_t Q + \zeta_x E + \zeta_y F + \zeta_z G \right) - \frac{1}{J}\left(\zeta_x E_v + \zeta_y F_v + \zeta_z G_v \right)$$

$$\tag{2}$$

$$Q = \begin{array}{c} \rho \\ \rho u \\ \rho v \\ \rho w \\ e \end{array} \qquad , \qquad E = \begin{array}{c} \rho u \\ \rho u^2 + P \\ \rho uv \\ \rho uw \\ (e + P)u \end{array} \tag{3}$$

$$F = \begin{array}{c} \rho v \\ \rho uv \\ \rho v^2 + P \\ \rho vw \\ (e + P)v \end{array} \qquad , \qquad G = \begin{array}{c} \rho w \\ \rho uw \\ \rho vw \\ \rho w^2 + P \\ (e + P)w \end{array}$$

In these equations, ρ is the density, u, v, and w are the components of the velocity in the x, y, z directions, respectively, and e is the total internal energy per unit volume. The pressure, P, is related to the energy by

$$P = (\gamma - 1)\left[e - \frac{1}{2}\rho\left(u^2 + v^2 + w^2 \right) \right] \tag{4}$$

$$F_v = \begin{array}{c} 0 \\ \tau_{xx} \\ \tau_{xy} \\ \tau_{xz} \\ \frac{\gamma}{P_r} K \frac{\partial T}{\partial x} + u\tau_{xx} + v\tau_{xy} + w\tau_{xz} \end{array}$$

$$G_v = \begin{array}{c} 0 \\ \tau_{xy} \\ \tau_{yy} \\ \tau_{yz} \\ \dfrac{\gamma}{P_r} K \dfrac{\partial T}{\partial y} + u\tau_{xy} + u\tau_{yy} + w\tau_{yz} \end{array} \tag{5}$$

$$H_v = \begin{array}{c} 0 \\ \tau_{xz} \\ \tau_{yz} \\ \tau_{zz} \\ \dfrac{\gamma}{P_r} K \dfrac{\partial T}{\partial z} + u\tau_{xz} + v\tau_{yz} + w\tau_{zz} \end{array}$$

$$\xi_t = -\left(x_t \xi_x + y_t \xi_y + z_t \xi_z \right)$$

$$\eta_t = -\left(x_t \eta_x + y_t \eta_y + z_t \eta_z \right)$$

$$\zeta_t = -\left(x_t \zeta_x + y_t \zeta_y + z_t \zeta_z \right)$$

where

$\xi = \xi(x,y,z,t)$ = Streamwise (marching) direction

$\eta = \eta(x,y,z,t)$ = Normal direction

$\zeta = \zeta(x,y,z,t)$ = Spanwise or circumferential direction

J is the Jacobian of the transformation given by

$$J = \partial(\xi, \eta, \zeta) / \partial(x, y, z)$$

$$\tau_{xx} = \frac{2}{3} \mu \left(2\frac{\partial u}{\partial x} - \frac{\partial v}{\partial y} - \frac{\partial w}{\partial z} \right) \qquad \tau_{xy} = \mu \left(\frac{\partial u}{\partial y} + \frac{\partial v}{\partial x} \right)$$

$$\tau_{yy} = \frac{2}{3} \mu \left(2\frac{\partial v}{\partial y} - \frac{\partial u}{\partial x} - \frac{\partial w}{\partial z} \right) \qquad \tau_{zx} = \mu \left(\frac{\partial u}{\partial z} + \frac{\partial w}{\partial x} \right) \tag{6}$$

$$\tau_{zz} = \frac{2}{3} \mu \left(2\frac{\partial w}{\partial z} - \frac{\partial u}{\partial x} - \frac{\partial v}{\partial y} \right) \qquad \tau_{yz} = \mu \left(\frac{\partial v}{\partial z} + \frac{\partial w}{\partial y} \right)$$

where,

$\mu = \mu_L + \mu_T$ afterbody calculations

$\mu = \mu_L$ jet and nozzle calculations

μ_L and μ_T are the laminar and turbulent viscosity respectively. In the present investigation, the turbulent viscosity is evaluated using two algebraic turbulence models which are described subsequently.

6

The Parabolized Navier-Stokes (PNS) equations are obtained from the governing equations when the unsteady terms are omitted and the following assumptions are enforced:

1. The streamwise velocity component is everywhere greater than zero.

2. The pressure gradient term in the streamwise direction $\partial P/\partial\xi$ is either omitted or treated with other techniques to avoid a complex eigenvalue.

In the present investigation, the technique of Vigneron et. al.[37] is adopted to suppress the departure solutions associated with the elliptic behavior of the equations. Vigneron et. al.[37] show that PNS equations are hyperbolic-parabolic provided that the streamwise convected flux vector is replaced by

$$\hat{E}=\left[\rho\hat{U},\rho u\hat{U}+S_x\,\omega P,\rho v\hat{U}+S_y\omega P,\rho w\hat{U}+S_z\omega p,(e+P)\hat{U}\right] \tag{7}$$

where

$$\omega = 1 \qquad\qquad M_\xi \geq 1$$

$$=\frac{\sigma\gamma M_\xi^2}{1+(\gamma-1)M_\xi^2} \qquad M_\xi < 1$$

and, σ is a safety factor to account for the nonlinearity of the governing equations. A value of 0.95 is used in the present calculations.

3. Turbulence Models

The Baldwin-Lomax, Johnson-King, and Goldberg turbulence models (for wall boundary problems) and mixing length turbulence models (for shear flow problems) are briefly described in this section.

3.1 Baldwin-Lomax Model

The Baldwin-Lomax[10] model is an algebraic two-layer turbulence model which follows the pattern adopted by Cebeci[11]. The model is developed for thin-layer, two- and three-dimensional calculations. The turbulent viscosity is evaluated as follows:

$$\mu_t = (\mu_t)_i \qquad\qquad \eta \leq \eta_{cros}$$
$$\mu_t = (\mu_t)_o \qquad\qquad \eta > \eta_{cros}$$

where η is the normal distance from the afterbody surface and η_{cros} is the smallest value of η at which values of $(\mu_t)_i$ and $(\mu_t)_o$ are equal. For the inner-layer:

$$(\mu_t)_i = \rho \iota^2 \, |\omega| \tag{8}$$

where, $\iota = k\eta \left[1 - \exp\left(-\eta^+/A^+ \right) \right]$

and, $k = 0.4$, $A^+ = 26$

$$\eta^+ = \frac{\rho_w \tau_w \eta}{\mu_w} \tag{9}$$

where τ_w = wall shear stress

$|\omega|$ is the magnitude of the vorticity.

There are two different ways to calculate $|\omega|$; the three-dimensional form:

$$|\omega|_{3D} = \left[\left(\frac{\partial u}{\partial y} - \frac{\partial v}{\partial x} \right)^2 + \left(\frac{\partial v}{\partial z} - \frac{\partial w}{\partial y} \right)^2 + \left(\frac{\partial w}{\partial x} - \frac{\partial u}{\partial z} \right)^2 \right]^{1/2} \tag{10a}$$

and the thin-layer approximation

$$|\omega|_{T-L} = \left[\left(\eta_y \frac{\partial u}{\partial \eta} - \eta_x \frac{\partial v}{\partial \eta} \right)^2 + \left(\eta_z \frac{\partial v}{\partial \eta} - \eta_y \frac{\partial w}{\partial \eta} \right)^2 + \left(\eta_x \frac{\partial w}{\partial \eta} - \eta_z \frac{\partial u}{\partial \eta} \right)^2 \right]^{1/2} \tag{10b}$$

For the outer-layer:

$$(\mu_t)_o = K C_{cp} \, \rho \, F_{wake} \, F_{kleb} \, (\eta) \tag{11}$$

where, $C_{cp} = 1.6$, $k = 0.018$

$$F_{wake} = \text{the smaller of} \quad \begin{array}{l} \eta_{max} \; F_{max} \\[6pt] C_{wk} \eta_{max} U / F_{max} \end{array}$$

$U = u^2 + v^2 + w^2$, $C_{wk} = 0.25$

η_{max} is the η location corresponded to the maximum value (F_{max}) where F is calculated by

8

$$F(\eta) = \eta |\omega| \left[1 - \exp\left(-\eta^+/A^+ \right) \right]$$

(12)

and

$$F_{kleb} = \left[1 + 5.5 \left(\frac{C_{kleb} \eta}{\eta_{max}} \right)^6 \right]^{-1}$$

(13)

$C_{kleb} = 0.3$

3.2 Johnson-King Model

The Johnson-King model[12,13] is a two-layer hybrid eddy-viscosity/Reynolds-shear-stress model. A simplified ordinary differential equation for the maximum Reynolds shear stress (τ_m) is used to determine the change in the turbulent viscosity in the streamwise direction. The initial values of the Reynolds shear stress (along each line normal to the afterbody) have to be evaluated with some other approaches. The original model was developed for 2-D flows in which a 1-D equation for τ_m is to be solved. Abid[19] and Abid et. al.[14] extended the Johnson-King model[12] for the application to 3-D flows. In the Johnson-King model, the turbulent viscosity is expressed as

$$\mu_t = (\mu_t)_o \left[1 - \exp\left(-(\mu_t)_o / (\mu_t)_i \right) \right]$$

(14)

$$(\mu_t)_i = k\eta \tau_m^{1/2} \left[1 - \exp\left(-\eta_i^+ / A_i^+ \right) \right]$$

(15)

where

$$\eta_i^+ = \rho\eta \tau_{max}^{1/2} / \mu_t$$

$$A_i^+ = 17$$

τ_{max} = maximum Reynolds shear stress/density

$$\tau = \mu_t |\omega|/\rho$$

(16)

The outer eddy viscosity is the same as the one used for the Baldwin-Lomax model (equation 11) but multiplied by a correction factor σ. However, k takes a value of 0.0168 as suggested by Abid et. al.[14]. The σ factor provides a link between the eddy viscosity evaluated by equation (16) and τ_m. τ_m is evaluated by solving the 2-D ordinary differential equation, which can be written in the following finite volume form:

$$\delta_\xi g + \frac{W_m}{U_m} \delta_\zeta g + \Gamma = 0 \tag{17}$$

where

$$U_m = R_x u_m + R_y v_m + R_z w_m$$

$$W_m = T_x u_m + T_y v_m + T_z w_m$$

$$\Gamma = \frac{a_1}{2L_m}\left(\frac{g}{g_{eq}} - 1\right) - \frac{C_D L_m |1 - \sigma^{1/2}|}{\delta a_1 (0.7 - \eta_m/\delta)} \frac{Vol}{U_m} \tag{18}$$

where $a_1 = 0.25$, $C_D = 0.5$

$L_m = min (0.4\,\eta_m,\ 0.09\delta)$

$g = \tau_m^{-1/2}$

First, the Baldwin-Lomax model is used to supply the initial values for τ_m at each streamwise location, and σ is set to 1. Then, at the following time steps, equation (17) is solved for τ_m using an upwind-scheme, and σ is updated as follows

$$\sigma^{t + \Delta t} = \sigma^t \tau_m \rho_{max}/(\mu_t |\omega|)_{max} \tag{19}$$

In the region where σ is less than unity, the value of $|1 - \sigma^{1/2}|$ (equation 14) is set to zero.

3.3. Goldberg Modification

Goldberg[15] and Goldberg and Chakravarthy[16] introduced a modification for boundary layer turbulence models, which is designed to simulate the separation bubble

10

in the flow. The modification consists of a simple formula for the distribution of the eddy viscosity within the separation bubble. The Baldwin-Lomax model is used outside the separation bubble and the edge of the separation region "η_s" is treated as a wall boundary. Thus, the η in equations 9, 11, 12 and 13 is replaced by "$\eta-\eta_s$".

For high Reynolds number flows, Goldberg and Chakravarthy[16] show that the viscosity in the separation regions can be evaluated as

$$(\mu_t)_s = C_1 u_s \eta_s \sqrt{\rho_w \rho} \left[A(\eta / \eta_s) + B \right] \sqrt{G} \qquad 0 < \eta < \eta_s \qquad (20)$$

and

$$(\mu_t)_v = C_2 u_s \eta_s \sqrt{\rho_w \rho} \qquad \eta_s \leq \eta < \eta_{cr} \qquad (21)$$

where

$$G = [1 - e^{-\phi(\eta/\eta_s)^2}] / [1 - e^{-\phi}]$$

$$A = -\left(C_\mu / 2 \right)^{9/5}, B = \left(\frac{C_\mu}{2} \right)^{3/5} - A$$

$$u_s = \sqrt{\frac{u_{t,m} \omega_{max}}{\rho}}$$

$$\mu_{t,m} = \mu_t |_{\omega_{max}}$$

$C_1 = 0.353, C_2 = 0.188, \phi = 0.5, C_\mu = 0.7$

In the separation layer, equation (16) is used up to η_{cr}, the smallest value of η at which values from equation (20) and Baldwin-Lomax model are equal. Beyond η_{cr}, the Baldwin-Lomax model is used.

3.4 Mixing Length Model (ML)

This is an algebraic eddy-viscosity turbulence model which is based on the Prandtl hypothesis. The turbulence viscosity is evaluated as

11

$$\mu_T = \rho \iota^2 \, |\omega| \qquad (22)$$

where ι is the turbulence length scale,

$$\iota = 0.11 \eta_G$$

$$\eta_G = \eta_2 - \eta_1$$

where at η_1

$$\frac{U - U_\infty}{U_0 - U_\infty} = 0.1 \qquad (23a)$$

and at η_2

$$\frac{U - U_\infty}{U_0 - U_\infty} = 0.9 \qquad (23b)$$

where $U = \xi_x u + \xi_y v + \xi_z w$

is the contravarient velocity component in the streamwise directions, U_∞ is the external flow velocity and U_0 is the jet centerline velocity.

3.5 Compressibility-Corrected Mixing Length Model (ML-CC).

It is well known that turbulent mixing rates are reduced for supersonic flows in comparison to subsonic flows. Chuech et. al.[17] introduced a compressibility corrections factor and used it to modify the turbulent viscosity:

$$\mu_t = K \rho \iota \, |\omega| \qquad (24)$$

where k

= 1.0		$M_c < 0.55$
= 2.03 - 1.87M_c	for	$0.55 \leq M_c \leq 0.95$
= 0.25		$M_c > 0.95$

where M_c is the connective Mach number of the mixing layer.

4. Computational Methods

The three computational schemes presented in this report are basically implicit, upwind, and constructed using a finite volume method. The diffusion terms

are centrally differenced and the inviscid flux terms are upwind differenced in these schemes. Associating the subscripts i,k,j with ξ, η, ζ directions, a numerical approximation to Eq. (1) may be written in the following form:

$$\left(\hat{Q}_{i,k,j}\right)_t + \hat{E}^{n+1}_{i+\frac{1}{2},k,j} - \hat{E}^{n+1}_{i-\frac{1}{2},k,j} + \hat{F}^{n+1}_{i,k+\frac{1}{2},j} - \hat{F}^{n+1}_{i,k-\frac{1}{2},j} + \hat{G}^{n+1}_{i,k,j+\frac{1}{2}} - \hat{G}^{n+1}_{i,k,j-\frac{1}{2}} = 0 \qquad (25)$$

The fluxes at (n + 1 time iteration) are linearized as

$$\hat{E}^{n+1} = \hat{E}^n + \frac{\partial \hat{E}^n}{\partial Q} \Delta Q$$

$$\hat{F}^{n+1} = \hat{F}^n + \frac{\partial \hat{F}^n}{\partial Q} \Delta Q$$

$$\hat{G}^{n+1} = \hat{G}^n + \frac{\partial \hat{G}^n}{\partial Q} \Delta Q$$

Then, equation (25) is written as,

$$\hat{E}^{n+1}_{i+\frac{1}{2},k,j} - \hat{E}^{n+1}_{i-\frac{1}{2},k,j} = \left\{\hat{E}^+\left(Q^-\right) + \hat{E}^-\left(Q^+\right)\right\}^n_{i+\frac{1}{2},k,j}$$

$$- \left\{\hat{E}^+\left(Q^-\right) + \hat{E}^-\left(Q^+\right)\right\}^n_{i+\frac{1}{2},k,j}$$

$$+ \left\{\frac{\partial \hat{E}^+\left(Q^-\right)}{\partial Q}\Delta Q^- + \frac{\partial \hat{E}^-\left(Q^+\right)}{\partial Q}\Delta Q^+\right\}_{i+\frac{1}{2},k,j}$$

$$+ \left\{\frac{\partial \hat{E}^+\left(Q^-\right)}{\partial Q}\Delta Q^- + \frac{\partial \hat{E}^-\left(Q^+\right)\Delta Q^+}{\partial Q}\Delta Q^+\right\}_{i-\frac{1}{2},k,j}$$

$$(26)$$

13

In the present code, two flux-splitting schemes are used to construct the convective flux terms in equation (26).

The variables Q^+, Q^- are defined by an upwind biased one parameter family

$$Q^-_{i+\frac{1}{2},k,j} = Q_{i,k,j} + \frac{\phi}{4} \left\{ \left(1 - k_\xi\right) \nabla_\xi + \left(1 + k_\xi\right) \Delta_\xi \right\} Q_{i,k,j}$$

$$\tag{27}$$

$$Q^+_{i+\frac{1}{2},k,j} = Q_{j+1,k,j} - \frac{\phi}{4} \left\{ \left(1 + k_\xi\right) \nabla_\xi + \left(1 - k_\xi\right) \Delta_\xi \right\} Q_{i,k,j}$$

These variables can be either the conservative or primitive variables. Also, Q+ and Q- represent the right and left variables, respectively, in reference to the cell face.

where

$$\Delta_\xi Q_{i,k,j} = Q_{i+1,k,j} - Q_{i,k,j}, \quad \Delta_\xi Q_{i,k,j} = Q_{i,k,j} - Q_{i-1,k,j}$$

$\phi = 0$ first order fully upwind

$k_\xi = -1$

$\phi = 1$ second order fully upwind

$k_\xi = \dfrac{1}{3}$

$\phi = 1$ third order biased upwind

However, to ensure monotonic interpolation for the third order interpolation in the vicinity of a shock, a min mod limiter is used as follows:

$$\nabla Q = \text{min mod} \left(\nabla Q, b \Delta Q\right)$$

$$\tag{28}$$

$$\Delta Q = \text{min mod} \left(\Delta Q, b \nabla Q\right)$$

where b is a compression parameter, $b = \dfrac{3 - k_\xi}{1 - k_\xi}$

It should be mentioned that the splitting procedures are only used for the inviscid convection parts of the flux vectors $\left(\hat{F} \text{ and } \hat{G}\right)$. A second order, central difference is used to represent the diffusion (viscous) terms.

$$\left(\frac{I}{\Delta t}\,\text{Vol} + B_\xi + B_\eta + B_\zeta\right)\Delta Q_{i,k,j}^{n+1}$$

$$+A_\xi\,\Delta Q_{i-1}^{n+1} + A_\eta\Delta Q_{k-1}^{n+1} + A_\zeta\Delta Q_{j-1}^{n+1}$$

$$\hspace{10cm}(29)$$

$$+C_\xi\,\Delta Q_{i+1}^{n+1} + C_\eta\Delta Q_{k+1}^{n+1} + C_\zeta\Delta Q_{j+1}^{n+1} = \text{R.H.S}^n$$

$$A_\zeta = \left(J_1^+\right)_{j-\frac{1}{2}} - V_1\left(j - \frac{1}{2}, j - 1\right), B_\zeta = \left(J_1^+\right)_{j+\frac{1}{2}} - \left(J_1^-\right)_{j-\frac{1}{2}} + V_1\left(j + \frac{1}{2}, j\right) - V_1\left(j - \frac{1}{2}, j\right),$$

$$C_\zeta = \left(J_1^-\right)_{j+\frac{1}{2}} + V_1\left(j - \frac{1}{2}, j\right)$$

$$A_\eta = \left(J_2^+\right)_{k-\frac{1}{2}} - V_2\left(k - \frac{1}{2}, k - 1\right),$$

$$B_\eta = \left(J_2^+\right)_{k+\frac{1}{2}} - \left(J_2^-\right)_{k-\frac{1}{2}} + V_2\left(k + \frac{1}{2}, k\right), - V_2\left(k - \frac{1}{2}, k\right)$$

$$C_\eta = \left(J_2^-\right)_{k+\frac{1}{2}} - V_2\left(k + \frac{1}{2}, k + 1\right)$$

$$A_\xi = \left(J_3^+\right)_{i-\frac{1}{2}}$$

$$B_\xi = J_3^+{}_{i+\frac{1}{2}} + \left(J_3^-\right)_{i-\frac{1}{2}}$$

$$C_\xi = \left(J_3^-\right)_{i+\frac{1}{2}}$$

15

$J_1^\pm, J_2^\pm, J_3^\pm, V_1$ and V_2 are completely described in Ref (1).

The implicit upwind/relaxation algorithm of Newsome et. al.[38] is used to solve the governing equations. This can be achieved through a series of alternative sweeps in the streamwise direction. For a forward sweep, $\Delta Q^n_{i-1,k,j}$ is known and $\Delta Q^{n+1}_{i+1,k,j}$ is set to zero. For a backward sweep, $\Delta Q^n_{i+1,k,j}$ is known and $\Delta Q^{n+1}_{i-1,k,j}$ is set to zero.

Finally, equations (29) are approximately factored and can be written in the following compact form:

$$\left(L + \delta_n\left(\frac{\partial \hat{F}}{\partial Q} + \frac{\partial \hat{F}_v}{\partial Q}\right)\right)L^{-1}\left(L + \delta_\zeta\left(\frac{\partial \hat{G}}{\partial Q} + \frac{\partial \hat{G}_v}{\partial Q}\right)\right)\Delta Q^{n+1} = \text{R.H.S} \tag{30}$$

where,

$$L = \frac{\text{Vol}}{\Delta t} + B_\xi$$

4.1 van Leer flux vector-splitting scheme

The first of the two schemes is the van Leer[8] flux-vector-splitting method. The inviscid terms of the flux vectors $\left(\hat{E}, \hat{F} \text{ and } \hat{G}\right)$ are split according to their contravariant Mach number.

$$\left(M_\xi, M_\eta \text{ and } M_\zeta\right), \text{ defined as } M_\xi = \frac{\overline{U}}{a}, M_\eta = \frac{\overline{V}}{a} \text{ and } M_\zeta = \frac{\overline{W}}{a} \tag{31}$$

where

$$\overline{U} = \left(S_x u + S_y v + S_z w\right)/S$$

$$\overline{V} = \left(R_x u + R_y v + R_z w\right)/R$$

$$\overline{W} = \left(T_x u + T_y v + T_z w\right)/T$$

$$S^2 = S_x^2 + S_y^2 + S_z^2$$

$$R^2 = R_x^2 + R_y^2 + R_z^2 \quad \text{and} \quad T^2 = T_x^2 + T_y^2 + T_z^2$$

As an example, for supersonic flows in the x direction

$$\hat{E}^+ = \hat{E}, \quad \text{and} \quad \hat{E}^- = 0, \quad \text{for} \quad M_\xi > 1$$

$$\hat{E}^+ = 0, \quad \text{and} \quad \hat{E}^- = \hat{E}, \quad \text{for} \quad M_\xi < -1$$

(32)

and for subsonic flows, $-1 < M_\xi < 1$

$$\hat{E}^\pm = S \begin{Bmatrix} E_{mass}^\pm \\[2ex] E_{mass}^\pm \left\{ S_x \left(-\overline{U} \pm 2a\right) / \gamma S + u \right\} \\[2ex] E_{mass}^\pm \left\{ S_x \left(-\overline{U} \pm 2a\right) / \gamma S + v \right\} \\[2ex] E_{mass}^\pm \left\{ S_z \left(-\overline{U} \pm 2a\right) / \gamma S + w \right\} \\[2ex] E_{energy}^\pm \end{Bmatrix}$$

where

$$E_{mass}^\pm = \pm \rho a \left(M_\xi \pm 1 \right)^2 / 4$$

$$E_{energy}^\pm = E_{mass}^\pm \left\{ -(\gamma - 1)\overline{U}^2 \pm 2(\gamma - 1)\overline{U} a + 2 a^2 \right\} / \left(\gamma^2 - 1 \right) + \frac{1}{2} \left(u^2 + v^2 + w^2 \right)$$

(33)

4.2 Roe's flux-difference-splitting scheme

The second scheme is the Roe's flux-difference-splitting method[9], which solves the approximate Riemann problem. For example, the interface flux in the streamwise direction is evaluated as,

17

$$\hat{E}_{i+\frac{1}{2}} = \frac{1}{2}\left[\hat{E}(Q_L) + \hat{E}(Q_R) - |\tilde{A}|(Q_R - Q_L)\right]_{i+\frac{1}{2}} \tag{34}$$

where Q_L (Q^-) and Q_R (Q^+) are either primitive or conservative variables to the left and

the right of the cell faces, and $\tilde{A}$ is the Roe-averaged flux Jacobian matrix:

The last term in equation (34) $|A|$ $(Q_R - Q_L)$ is defined as:

$$|\tilde{A}|(Q_R - Q_L) = \begin{bmatrix} \alpha_4 \\ \tilde{u}\alpha_4 + k_x\alpha_5 + \alpha_6 \\ \tilde{u}\alpha_4 + k_y\alpha_5 + \alpha_7 \\ \tilde{w}\alpha_4 + k_z\alpha_5 + \alpha_8 \\ \tilde{H}\alpha_4 + \alpha_5\tilde{u} + \alpha_8\overline{u} + \alpha_7\overline{v} + \alpha_8\overline{w} - \frac{\gamma\tilde{c}^2}{\gamma-1} \end{bmatrix} \tag{35}$$

$$\tilde{u} = \frac{u_L\sqrt{\rho_L} + u_R\sqrt{\rho_R}}{\sqrt{\rho_L} + \sqrt{\rho_R}} \tag{36}$$

Also, $\hat{p}, \hat{v}, \hat{w}$ and $\hat{H}$ are evaluated using formulas similar to eq. (36) and

$$\tilde{c}^2 = (\gamma - 1)\tilde{H} - \frac{\tilde{u}^2 + \tilde{v}^2 + \tilde{w}^2}{2} \tag{37}$$

where

$$\alpha_1 = K|\tilde{\tilde{u}}|\left(\Delta\rho - \frac{\Delta P}{\tilde{c}^2}\right) \tag{38}$$

$$\alpha_2 = \frac{1}{2\tilde{c}^2}K|\tilde{\tilde{u}} + \tilde{c}|(\Delta P + \rho\tilde{c}\,\Delta\,\overline{u})$$

$$\alpha_3 = \frac{1}{2\tilde{c}^2}K|\tilde{\tilde{u}} - \tilde{c}|(\Delta P - \rho\tilde{c}\,\Delta\,\overline{u})$$

$$\alpha_4 = \alpha_1 + \alpha_2 + \alpha_3$$

$$\alpha_5 = \tilde{c}(\alpha_2 - \alpha_3)$$

$$\alpha_6 = K|\tilde{\tilde{u}}|\tilde{p}\,(\Delta u - k_x\,\Delta\,\overline{u})$$

$$\alpha_7 = K|\bar{\bar{u}}|\bar{\rho}\left(\Delta v - k_y\,\Delta\bar{u}\right)$$

$$\alpha_8 = K|\bar{\bar{u}}|\bar{\rho}\left(\Delta w - k_z\,\Delta\bar{u}\right)$$

and

$$K = \left|\frac{\sqrt{k_x^2 + k_y^2 + k_z^2}}{J}\right|$$

For fully supersonic flow, the information (disturbance) can only travel in the flow direction according to equation (34)

$$\hat{E}_{i+1/2,k,j} = \left[\hat{E}\left(Q^-\right)\right]_{i+1/2,k,j} \qquad\qquad M_\xi > 1 \qquad\qquad (39)$$

$$\delta_\xi(\hat{E}) \stackrel{\Delta}{=} \text{Backward difference}$$

where $\bar{M}_\xi$ is the average Mach number evaluated using the Roe-averaged method. The same result is achieved by setting the state variables at the $i + 1$ and $i + 2$ planes to be equal to the ones at the J-plane,

$$Q_{i+2} = Q_{i+1} = Q_i \qquad\qquad \bar{M}_\xi > 1 \qquad\qquad (40)$$

For a large number of supersonic/subsonic mixing flow problems, the downstream influence (contributed from the subsonic regions) can be neglected when compared with the upstream effect. For these cases, equation (18) can even be used in the subsonic regions to obtain an accurate solution.

With this approach, a simple modification to the Navier-Stokes solvers can be made and a wide range of problems can be simulated with a single sweep. This approach does not require any changes in the governing equations restrictions on the mean values of the streamwise velocity.

For a time dependent solution, either the flux-vector-splitting or the flux-difference-splitting scheme is used in all three computational directions. However, these schemes are only used in η and ζ directions to obtain a space marching solution. In this case, either a PNS formulation or modified Roe's scheme is used to calculate the fluxes in the ξ direction.

With alternate forward and backward relaxation sweeps, a time-dependent solution can be obtained for general flow problems. A one-sweep solution can be obtained for supersonic/subsonic mixing problems using either the PNS formulation or the modified Roe's scheme. In these procedures, a local time-like iteration is used until the residual at the local plane is reduced four orders of magnitude. Space marching solutions require much less computational time than fully time-dependent solutions, and these can also be used as initial conditions to reduce the computational effort required by time-dependent solutions.

5. Adaptive Grid Technique

In the present report, the adaptive grid technique introduced by Pao and Abdol-Hamid[5] is used to analyze the aerodynamic characteristics of shock containing single jets. This strategy is based upon the monitoring surface and equidistribution concept by Eiseman[39-41]. Flow variables are used as the monitoring functions for grid adaptation in the computational domain of interest. Grid density is governed by the geometric properties of the monitoring functions. In this method, a template grid is first generated by a geometrical function which concentrates the grid points to a circular zone surrounding the jet plume while leaving an adequate number of grid points in the farfield computational domain. For the jet exit plane, this initial grid is adapted to axial velocity (representative of the shear layer) and the pressure (representative of the shock location). Adaptive grid for subsequent axial planes are generated by using the adapted grid in the previous plane as its template.

20

6. Boundary Conditions

6.1 Multiblock/Multizone Methodology

The present multiblock/multizone strategy allows a great deal of topological flexibility. As long as there is no change in grid topology (polar or cartesian) or distribution (fine or coarse), additional blocks or zones are not necessary when the boundary condition changes along a block face. Each of the six block faces can have any combination of boundary conditions. Boundary conditions can be either a direct communication at the block interface or a regular boundary condition (inflow, outflow, reflection, symmetry wall or extrapolation). With this flexibility, the solver requires fewer blocks and zones which significantly reduces the overhead required for the communication between block/zone interfaces.

A typical computational domain (figure 1) may contain zones, blocks and partitions. The relations between zones, blocks and partitions are defined as follows:

Zone (Z_m): parts of the computational domain organized linearly along the i-direction. Each zone may contain multiple blocks. Each block within a zone can interface with blocks in adjacent zones where mixed boundary conditions are allowed. Communications at the zone level are restricted to face 5 ($i_{zm} = 1$) which communicates with face 6 of zone Z_{m-1}, and face 6 ($i=i=imax_{zm}$) which communicates with face 5 of the next zone Z_{m+1}. Blocks within a zone can terminate only at face 6 of the zone. Face 5 of zone 1 and face 6 of the last zone of the computational domain can have any combination of the regular boundary conditions.

Block (B_n): subsection of Zm, can start at any i-location ($IMIN_{Zm} < i_{Bn} < IMAX_{Zm}$) with different regular boundary conditions and interface with any other block (if needed) at faces 1,2,3 and 4. Face 5 and 6 can communicate with another from zone Z_{m-1} and Z_{m+1} with any combination of regular boundary conditions. Face 1,2,3, and 4 are defined as follows: for $i = I_{Bn}$, $imax_{Zm}$

face 1 j= jmax, k=1, kmax

face 1 j= jmax, k=1, kmax

face 2 j=jmin, k=1, kmax

face 3 k=kmin, j=1, jmax

face 4 k=kmax, j=1, jmax

The interface between blocks can be of any direction or order (coarse to fine grid). Any of the four faces (1-4) in one block can communicate with any number of blocks and different faces in any order. With this flexibility, there is no need to break a block into a number of blocks on account of communications with more than one block or mixed boundary conditions on a block interface. The only computational effort is setting the correct boundary conditions for each of the four faces of a block.

Partition (P_1): subsection of a block within a zone, which can start any i-location. The partition allows the user to change boundary conditions without adding an extra zone. Any of the four faces boundary conditions can be changed and a turbulent or laminar solution can be selected for each partition.

Different examples of using the present multiblock/multizone methodology has been mentioned in Section 1. This method will simplify grid generation by reducing the number of blocks and zones needed to describe a complex computational domain and by giving the users more flexibility in breaking the computational domain into simple sections.

6.2 Regular Boundary Conditions.

Regular boundary conditions are inflow, outflow, reflection, symmetry, wall and extrapolation. In the following equations, a boundary point is denoted by "η", and the factitious image point is denoted by "Γ". Boundary points (f) are calculated as follows:

a) Inflow/Outflow Boundary

The treatment of this boundary is based on Riemann invariants for a one-dimensional flow. Riemann Invariants can be defined as

22

$$\hat{P} = \overline{V}_\eta \pm \frac{2}{\gamma - 1} a_\eta$$

$$\hat{Q} = \overline{V}_\eta \mp \frac{2}{\gamma - 1} a_\eta$$

where, + and - are the increasing and decreasing direction side of the η-direction, and side of the h-direction..

$$\overline{V}_\eta = k_x u + k_y v + k_z w$$

then, there follows:

$$V_R = \pm \frac{1}{2} \left(\hat{P} + \hat{Q} \right)$$

$$a_R = \mp \frac{\gamma - 1}{4} \left(\hat{P} - \hat{Q} \right)$$

The primitive flow variables can be written in a general form:

$$\{ \rho_f, u_f, v_f, w_f, p_f \}^T = \{ \overline{c}_1, \rho_\infty, u_\infty, v_\infty, w_\infty, \overline{c}_2 \rho_f \}^T + \overline{c}_3 \{ 0, k_x, k_y, k_z, 0 \}^T$$

where c_1, c_2, c_3 are given different values in various cases.

1) For inflow boundary conditions where $\overline{V}_R < 0$,

$$\overline{c}_3 = | \overline{V}_R - \overline{V}_\infty |$$

If the constant entropy restriction is applied, then

$$\overline{c}_1 = \left(\frac{a_R^2}{a_\infty^2} \right)^{\frac{1}{\gamma - 1}}, \overline{c}_2 = \frac{a_R^2}{\gamma}$$

otherwise, if the constant pressure restriction is applied, then

$$\overline{c}_1 = 1, \overline{c}_2 = \frac{a_\infty^2}{\gamma}$$

2) For outflow boundary conditions where , $V_R > 0$,

23

$$\bar{c}_3 = |\overline{V}_R - \overline{V}_\eta|$$

If the constant entropy restriction is applied, then

$$\bar{c}_1 = \left(\frac{a_R^2}{a_\eta^2} \frac{\rho_\eta}{\rho_R} \right)^{\frac{1}{\gamma-1}}, \bar{c}_2 = \frac{a_R^2}{\gamma}$$

constant pressure restriction

$$\bar{c}_1 = \frac{\gamma P_\infty}{a_R^2}, \bar{c}_2 = \frac{a_\infty^2}{\gamma}$$

b) <u>Reflection Boundary Condition</u>

There are three cases:

u-reflection

$$\{\rho_f, u_f, v_f, w_f, p_f\}^T = \{\rho_\eta, -u_\eta, v_\eta, w_\eta, p\}^T$$

v-reflection

$$\{\rho_f, u_f, v_f, w_f, p_f\}^T = \{\rho_\eta, u_\eta, -v_\eta, w_\eta, p\}^T$$

uv-reflection (quarter-plane polar grid)

$$\{\rho_f, u_f, v_f, w_f, p_f\}^T = \{\rho_\eta, -u_\eta, -v_\eta, w_\eta, p_\eta\}^T$$

c) <u>Symmetry Boundary Condition</u>

$$\{\rho_f, u_f, v_f, w_f, p_f\}^T = \{\rho_\eta, u_\eta, v_\eta, w_\eta, p_\eta\}^T$$

d) <u>Wall Boundary Condition</u>

At the wall, velocity normal to the wall surface is set to zero and no-slip conditions are imposed.

$$u = v = w = 0$$

The pressure on the wall surface is obtained by setting the pressure gradient to zero and adiabatic wall condition is employed for temperature.

e) <u>Extrapolation Boundary Condition</u>

There are three options:

zero-order

$$Q_f = Q_\eta$$

First-order

$$Q_f = 2 Q_\eta + Q_{\eta - 1}$$

Second-order

$$Q_f = 1.5 Q_\eta + 0.5 Q_{\eta - 1}$$

7. <u>Numerical Results and Discussions</u>

In this section, some of the computational options available in the PAB3-v2 code are used to simulate different flow problems. Three test cases, which use the multiblock/multizone, adaptive grid, time-dependent, space marching, parabolized Navier-Stokes, and turbulence model capabilities are presented. The average computational time on Cray-2 computer was 70 μ_s/grid point. The first test case is a group of calculations for underexpanded and overexpanded supersonic jets issued into still air from round, square, and elliptic nozzles using polar and Cartesian grids. The second case is the simulation of high pressure supersonic flow issued into still air from a two 5-tabs nozzles. Finally, subsonic and supersonic flows past a nonaxisymmetric afterbody and nozzle with either a solid simulated plume or a supersonic jet exhaust are computed and compared with experimental data.

7.1 <u>Supersonic jet plume</u>

The present three-dimensional code is used to predict the shock-cell and flow characteristics of both underexpanded and overexpanded supersonic jets issued into

2 5

still air. The present predictions for round nozzles are qualitatively compared with the experimental data of Love et. al.[42] for underexpanded supersonic jets. Quantitative comparisons are made with the experimental data of Norum and Seiner[43] for Mach 2 underexpanded and overexpanded supersonic jets issued from round nozzles. The present space marching scheme and adaptive grid are also used to simulate a supersonic underexpanded jet issued from both square and elliptic nozzles.

Since details of the initial jet profile are not available, all cases are computed using a top-hat profile at the jet exit. Free-stream Mach number in the ambient air is assumed to have a value of .05. Space marching and time-dependent solutions presented in this section are calculated by using the van Leer flux-vector-splitting scheme.

7.1.1 Polar Grid; Round Nozzle

In order to evaluate the capabilities of the present code, some of the important characteristics of mildly underexpanded supersonic jets are computed and compared with PNS predictions as well as the experimental data of Love et. al.[42]. These are the characteristics of the first shock-cell:

a) The location (ι) of the intersection between the incident shock wave

    jet centerline or the intersection can be a Mach disk..

b) The location of the expansion wave reflection at

    jet boundary, W.

Figure (2) shows a typical quarter plan polar grid used to calculate jet plume flow issued from a round nozzle. In figure (3), the computational results for ι/D and W/D are presented as a function of pressure ratio P_j / P_a, and compared with the experimental data of Love et. al[42]. The magnitude of ι and W increases with increasing pressure ratio for all three Mach numbers. Excellent agreement is achieved between the experimental data and computational results. In order to obtain PNS solutions, the highest applicable value of CFL number is approximately 5. By using the SMS technique, the

26

applicable values of CFL number can be as high as 30. Figure (4) shows a typical convergence history of the L-2 norm of the residual for SMS and PNS solutions. It is observed in this figure that the residual dropped by 10 orders of magnitude in less than 100 iterations for the SMS solution. However, the PNS solution behaves similar to the SMS (in the first 10 iterations), then the convergence rate deteriorates substantially. In most cases, SMS solutions using PAB3D-v2 take less than 80 percent of the computational time required by PNS to achieve a similar convergence history. For the free stream region surrounding a Mach 1.5 or 2.0 jet, PNS solutions were unstable for a CFL value higher than to a value of 2 and a Mach number less than 0.3. It is not clear why a converged solution for overexpanded supersonic jet cases could not be obtained using PNS methodology. On the other hand, converged solutions were obtained for a wide range of Mach numbers and pressure ratio using the SMS. It was noted that the PNS procedure was very sensitive to the inlet condition at the jet exit and that a large discontinuity always caused a departure solution.

These results indicate that SMS is a robust scheme which gives efficient and accurate solutions. These solutions can also be used as initial conditions for time-dependent Thin-Layer Navier-Stokes calculations which can reduce the number of iterations required for converged solutions[37]. SMS is to be used to calculate the test cases described in this section (section 7).

Figure (5) shows the periodic structure of the Mach contours for a sonic jet with different pressure ratios up to 10 jet-radii downstream of the jet exit. Higher pressure ratios produced less shock cells within the same distance. The sonic flow at the exit is expanded to a supersonic flow with a higher Mach number. The number of shock-cells decreases from 6 to 3 and the fully expanded Mach number increases from 1.1 to 2.0 as static pressure ratio is increased from 1.2 to 2.0.

7.1.1.1 Underexpanded Mach 2.0 Jet; $P_j/P_a = 1.45$

The space marching prediction using the modified Roe's scheme in the streamwise direction is compared with a fully time-dependent solution in this section. The grid size for this case was 151x11x41 and the time-dependent solution converged after 500 global iterations, which is approximately 2100 CPU Secs. On the other hand, the space marching solution took less than 100 CPU Secs on the Cray 2. Figure (6) shows the centerline pressure variation predictions using both time-dependent and space marching methods. The space marching technique gives a solution comparable to the time-dependent solution in less than 5 percent of the computer time. All the first and second shock-cell characteristics (spacing and strength) are captured with the space marching scheme.

Figure (7) shows a comparison of the predicted results using mixing length (ML) and mixing length with compressibility correction factor (ML-CC) turbulence models (SMS solution) with the measured streamwise pressure variation along the jet center line. The jet was operated at a pressure ratio of 1.45 corresponding to a fully expanded Mach number of 2.24 and was issued from convergent-divergent nozzle with a design Mach number of 2.

The measured static pressure distributions indicate a decay in the shock structure strength which is due to the interaction of shocks with the growing mixing layer. The ML turbulence model significantly overpredicts the shock-cell decay. It was expected that the incompressible turbulence model would not give a good prediction for compressible flow problems. The predicted result improved with the use of the compressibility correction factor of Chuech et. al.[17]. The computational result agrees reasonably well with the experimental data up to 30 jet-radii downstream of the jet-exit.

7.1.1.2 Overexpanded Mach 2 Jet; $P_j/P_a = .75$

Figure (8) shows the present code prediction capability for an overexpanded flow case and for ML-CC and ML turbulent solutions, respectively. The jet was operated at a pressure ratio of 0.75 and was issued from a convergent-divergent nozzle with a design Mach number of 2.

The code predicts the irregular centerline pressure data with remarkable precision. Both turbulence models give very similar pressure distributions and agree well with available data. This suggests that the mixing layer boundary does not reach the jet centerline. The code shows a sharp compression shock at the exit of jet as expected for this kind of flow. This increases the pressure downstream of the shock as shown in figure (8).

7.1.2 Cartesian Grid

A non-circular jet plume at off-design operating conditions (over- or underexpanded) may contain a very complex internal shock cell structure and the shear layer cross section goes through a complex sequence of shape transformations in the developing region of the jet plume. In this section, solutions obtained by using both fixed and adapted grids for underexpanded supersonic jet issued from round, square, and elliptic nozzles are presented. Cartesian topology is used for the grids because it offers excellent grid mobility for the adaptive grid cases. Calculations are made using the space marching scheme in the stream wise direction and van Leer flux-vector-splitting scheme in the crossplane directions with laminar flow assumption. Initial shear layer thickness is assumed to be .05 and .1 of the jet-radii for adaptive and fixed grid respectively. The test case is for an underexpanded supersonic jet with design Mach number of 2 and pressure ratio of 1.45.

7.1.2.1 Round Nozzle

With only 36x36 grid points, the adaptive grid scheme has sufficient grid density to represent the circular nozzle shear layer as shown in figure (9). As the shear layer

and shock front change their location, the grid will follow these changes. Fixed and adaptive grids were used for single and multiblock solutions of an underexpanded supersonic jet (P_j/P_a = 1.45). Figure (10) shows the centerline pressure distribution using a single-block solution with fixed and adaptive grid. The fixed grid solution is exactly the same as the results presented earlier using a polar grid topology. A secondary pressure rise at z/r_e = 4 appears stronger in the adaptive grid calculation (agrees with experimental data), and there is a slight upstream shift of the shock-cell position from the fixed to the adapted grid results. In general, the adapted grid solution agrees better with the experimental data. Figure (11) shows how well the adapted grid follows the shear layer and detected shock front locations as clearly described by the density contours shown in figure (12).

As can be noted in figure (9), cartesian grid topology wastes a large number of grid points in the farfield region. To eliminate this problem, a multiblock strategy can be used in the farfield region as shown in figure (13). In this figure, the computational domain is divided into three blocks with the adaptive grid procedure applied only to the first block (with jet plume). Block dimensions are 27x27, 4x13, and 4x18 which results in about 33 percent less grid points and, in turn, causes a large reduction in computational time when compared to the single block strategy. As shown in figure (14), the three-block solution, which uses less computational resources (memory and time), agrees well with the result produced using the single block strategy.

7.1.2.2 Square and Elliptical Nozzle

Figure (15) shows the initial adaptive grids generated for square and elliptic nozzle calculations. In the case of the square nozzle, the X-Z and Y-Z plane have similar shock-cell characteristics (density contours; figure (16)), to those presented for the round nozzle in figure (12). However, the cross section plane goes through a very complex transformation as the jet changes shape from square to round to diamond shape[3]. Similar observations are made by Anderson and Barber[23] for a supersonic

rectangular nozzle. Figure (17) shows the comparison between the adaptive and fixed grid predictions of the centerline pressure. The shock-cell spacing and strength are very similar to the round nozzle results. Again, the secondary pressure strength at X/r_e = 4 is much larger for the adaptive grid prediction than the fixed grid. In addition, there is another secondary pressure peak shown at X_{re} = 17 for the adaptive grid.

Figure (18) shows the density contours predictions for 2:1 elliptic nozzle. The shock-cell structure is very different from those presented for either the square or round nozzle. First, the minor axis grows each time that the shock reflected from the jet centerline intersects with the shear layer. At the same time, the major axis decays as the jet cross section transforms into a circular shape. Second, the shock front on the major axis plane (X-Z) is much stronger than the ones on the minor axis plane (Y-Z). Finally, the jet produces two different shock front structures associated with different scales (strength and space). It is believed that these structures have different centers which are not always located on the jet centerline (Z-axis). Figure (19) shows the centerline pressure distribution using fixed and adaptive grid solutions. The elliptic nozzle produces more shock-cells than either the round or square jet for a similar distance. In addition, the shock-cells have different centerline pressure characteristics (compare figure (19) with figures (10) and 17)). The adaptive grid solution predicts a large pressure peak for the first shock-cell whereas the fixed grid solution did not.

7.2 Supersonic Nozzle

In this section, the multiblock and partitioning options of PAB3D-v2 code are utilized to simulate a group of underexpanded supersonic jet flow which include both internal and external flow regions for a special family of jet nozzles. The examples are designed to show the flexibility of the PAB3D-v2 code in handling mixed boundary conditions over a block interface. The nozzle configuration can be described as a circular pipe section followed by five equally spaced tabs. Each tab is simply an extension of an arc segment of the circular pipe for a certain length in the downstream direction. Each arc

segment, representing the width of the tab, is 1/10 of the full circle. Two nozzle configurations are chosen. In the first case, the tabs are infinite in length in a direction parallel to the pipe centerline, (fig. 20). This nozzle will be referred to as the "infinite tab nozzle". Essentially, the entire flow field can be considered as internal to the nozzle although there is venting through the spaces between the tabs. In the second case, the tabs are chosen to be one pipe diameter i length, (Fig. 21). The nozzle exit plane is defined as the streamwise location at the end of the tabs. This configuration is called the "short tab nozzle". The flow region upstream of the nozzle exit plane is considered as the nozzle internal flow, and the flow downstream of the same plane is a free jet with a shear layer developing between the jet plume and the ambient free stream. Each of the two cases has an internal flow Mach number of 2 with an internal to external pressure ratio of 1.45 at the nozzle exit. The cross sectional computational domain of the nozzle requires the extensive use of multiblock strategy. Most CFD codes with multiblock capability do not have the capability of handling mixed interface condition at a block boundary. Therefore, these codes would have to divide this computational domain into at least 15 blocks as shown in figure (22) with the number of blocks increasing with the number of tabs. However, PAB3D-v2 code needs to use only 2 blocks to simulate this test case for any number of tabs. For the short tab nozzle test case, most CFD codes need another block to simulate the flow downstream of the nozzle exit. Using the partition option, the PAB3D-v2 code does not have any need for an extra block or zone. With this flexibility, more than a 20 percent reduction in grid points is achieved: the overhead due to interpolation between block boundaries is avoided; and the convergence rate of the solution is increased.

Figure (23) shows the Mach contours at different axial locations for the infinite tab nozzle test case. Initially, the flow escapes through the gaps between the 5 tabs and then the jet cross section changes into a pentagon shape connected at the midpoint of each tab. For, the short tab nozzle jet case (figure 24), the flow initially, goes through

the same transformation, but, the cross section changes its shape back to a circular one. Wiezien and Kibens[44] did a series of experiments for 1,2,4, and 8 tabs nonaxisymmetric nozzle-free jet. Their results indicate that multiple-tab nozzle plumes spread faster and have a lower core Mach number than the free-jet case for circular nozzles without tabs. The present predictions produce similar results to those reported in Ref. [44]. Figures (25) and (26) show the comparisons between centerline Mach number and pressure respectively for free-jet, nozzle-free jet, and nozzle test cases. The short tab nozzle case produces more shock-cells, decays faster, and has lower core Mach number than the free-jet described earlier in section 7 of this report. However, the infinite tab nozzle test case decays much faster, and has the lowest core Mach number of all cases considered.

7.3 Nonaxisymmetric Afterbody

In this section, the thin-layer Navier-Stokes equations are solved to simulate subsonic (M = 0.8) and supersonic (M = 1.2) flow cases over the nonaxisymmetric afterbody described in Ref. [45]. The third-order flux-difference splitting scheme of Roe is used to discretize the governing equations. In the subsonic case, jet-exhaust is included to utilize as an example to demonstrate the multiblock/multizone and partitioning options in the PAB3D-v2 code. The supersonic test case compares the performance of three different turbulence models in simulating a separated flow region.

First, for an external flow Mach number of 0.8 and the jet operating at Mach 2, a coarse grid topology is used for the calculation (figure (27)). A laminar flow assumption is made for the regions upstream of the body and downstream of the jet exit. A turbulent flow calculation using the Baldwin-Lomax turbulence model (Ref. (10)) is made in the region over the body. Three different multiblock/multizone configurations (1Z-2B, 2Z-2B, 2Z-3B) are used to grid this problem. The first configuration has one zone with two blocks. The first block has 64x32x10 grid points to represent the full external flow region with three partitions ending at i = 10, 50, and 64. The second block simulates the

33

jet-exhaust region with 14x10x21 grid points. In the second configuration, two-zone block topology is used. The first zone has one block (50x10x32) with two partitions ending at i = 10 and 50. The second zone has one block (14x10x52) which represents the internal and external flow regions downstream of the jet exit. The last configuration is similar to the second one except that the second zone splits into two blocks; one for the external flow region (14x10x32) and the other for the jet-exit region (14x10x21). It should be mentioned that CFD codes which permit only one boundary condition per block interface would require a minimum of 4 blocks to simulate the present test case. With the PAB3D-v2 flexibility in dealing with mixed boundary conditions, the present case can be solved with as little as two blocks.

Figure (28) shows the Mach contour predictions using the 1Z-2B topology (the other two topologies give exactly the same results). The smooth transition of the density contours between zone 1 and zone 2 is apparent in this figure. This transition is only possible because of the fully conservative nature of the zonal/block boundary scheme. The afterbody pressure distributions computed with the three different multiblock/multizone topologies are compared with experimental data in figure (29). All three calculations give exactly the same predictions (in less than 50 global iterations) and agree well with the experimental data.

The supersonic Mach 1.2 case is computed using three different turbulence models with a rectangular solid sting replacing the jet-exhaust. The three turbulence models are: the Baldwin-Lomax[10] model, the Johnson and King model[12-14] as extended to three-dimensional flows by Abid[13] and Abid, et. al.[14], and the Goldberg model[15-16]. Calculations are made with a single-zone/single-block topology with fine grid distribution (129x66x33).

The afterbody pressure distributions computed with the three different turbulence models (Baldwin-Lomax, Johnson-King, and Goldberg) are compared with

experimental data in figure (30). All three turbulence models predict the shock at approximately the correct axial location. The Johnson-King and Goldberg models, however, give shock locations slightly upstream which agree better with the data. Both the Johnson-King and Goldberg models give a much better prediction of the "pressure plateau" in the overcompression region. The Baldwin-Lomax model fails to predict the "pressure plateau". The Johnson-King model is presently the best in predicting the plateau.

While the Johnson-King model may be slightly better in predicting the "pressure plateau," it had to be calibrated for this flow regime. For flows with massive separation, Johnson[2] noticed that very large values of the ratio of the nonequilibrium maximum shear stresses were generated using the Johnson-King model. He suggested limiting this ratio should be limited to a maximum value of 3.0. For the present case, Abdol-Hamid and Compton[4] found that $\sigma < 2.5$ produces one of the best calculations when compared with the experimental data. Abid et. al. [16] used a limiting value of 4.0 in predicting the pressure distributions for the ONERA M6 wing. For the present calculation, it was noted (not shown) that the convergence with $\sigma = 2.5$ is slower than using the Baldwin-Lomax model. Again, Abid et. al.[16] made similar observations. An advantage of both the Goldberg and Baldwin-Lomax models is that they do not need to be calibrated for this flow.

8. Summary

The PAB3D-v2 code and its application to a variety of aerodynamic test problems have been discussed in this technical report. The code solves the three-dimensional simplified Navier-Stokes equations using the strong conservation form of the finite volume formulations. It uses two different flux-splitting schemes: van Leer's flux-vector-splitting and Roe's flux-difference-splitting. Also, the modified Roe's scheme is used to efficiently solve the governing equations in the steady state mode with a single global sweep. Several of the PAB3D-v2 options (multiblock/multizone,

adaptive grid, different turbulence models, and time-dependent and space marching numerical schemes) were applied to three different flow examples.

For the supersonic jet plume problem, the code uses its multiblock, adaptive grid, time-dependent and space marching strategies to predict the shock-cell structure for mildly underexpanded and overexpanded supersonic jet plumes. The jet is issued from round, square and 2:1 elliptic nozzles. The multiblock option reduces the computational time by at least 20 percent. The space marching strategy predicts exactly the shock-cell structure and when compared to a fully time-dependent strategy, requires less than 5 percent of the computational time to get a converged solution. The adaptive grid option enhances the prediction of the flow solver as it compares better with the experimental data.

For the vented supersonic nozzle test cases, the PAB3D-v2 code provides a very efficient multiblock interface strategy to solve the 5-tabs nozzle. Many CFD codes require a great number of blocks per tab to solve these kinds of problems with mixed boundaries. Only two blocks are required by PAB3D-v2 to solve this problem, regardless of the number of tabs and length.

The time-dependent option was utilized to simulate the flowfields around a nonaxisymmetric afterbody with external Mach numbers of 0.8 and 1.2. For the 0.8 Mach number case, the jet-exhaust was simulated with different multiblock/multizone topologies. The PAB3D-v2 code requires only two blocks to solve the jet-exhaust problem while many CFD codes need to break the flowfield into at least four blocks. Three different turbulence models were used and evaluated in solving the Mach 1.2 test case. The results of this study show that the Johnson-King and Goldberg turbulence models give a much better prediction of the shock location and pressure plateau in the separated region than the Baldwin-Lomax model.

In general, the PAB3D-v2 code can be used to simulate flowfields for complex aerodynamic configurations. Obviously, a detailed validation study using the several

options in the code needs to be made. However, there is still a need for more options and code upgrading. Upgrading the turbulence models from the algebraic level to the two-equation, multi-scale or algebraic Reynolds Stress level is needed to deal with 3D mixing and general aircraft configurations. Time-dependent adaptive grid methodology is needed for simulating vortical aspects of 3D mixing. Lastly, finite-rate chemistry with multiple species and multiphase solvers needs to be added to the code for solving jet plume and combustion problems.

<div align="center">9. <u>References</u></div>

1. Abdol-Hamid, K. S.: Development of Three-Dimensional Code for the Analysis of Jet Mixing Problem - Part I: Laminar Solution. NASA CR-4200, 1988.

2. Abdol-Hamid, K. S.: The Application of 3D Space Marching Scheme for the prediction of Supersonic Free Jets. AIAA Paper 89-2897, 1989.

3. Abdol-Hamid, K. S.: Three-Dimensional Calculations for Underexpanded and Overexpanded Supersonic Jet Flows. AIAA Paper 89-2196, 1989.

4. Abdol-Hamid, K. S. and Compton, W.B. III: Supersonic Navier-Stokes Simulations of Turbulent Afterbody Flows. AIAA Paper 89-2194, 1989.

5. Pao, S.; and Abdol-Hamid, K. S.: Application of a New Adaptive Grid for Aerodynamic Predictions of Shock Containing Single Jets. 26th AIAA/SAE/ASME/ASEE Joint Propulsion Conference, July 1990. AIAA Paper 90-2025, 1990.

6. Kutler, P.: A Perspective of Theoretical and Applied Computational Fluid Dynamics. AIAA Paper 83-0037, 1983.

7. Cosentino, G. B.; and Holst, T. L.: Numerical Optimization Design of Advanced Transonic Wing Configuration. AIAA Paper 85-0424, 1985.

8. van Leer, B.: Flux-Vector Splitting for the Euler Equations. ICASE Report 82-30, 1982.

9. Roe, P. L.: Characteristic Based Schemes for the Euler Equations. A Numerical Review of Fluid Mechanics, 1986, pp. 337-365.

10. Baldwin, B. S.; and Lomax, H.: Thin Layer Approximation and Algebraic Model for Separated Turbulence Flows. AIAA Paper 78-0257, 1978.

11. Cebeci, T.: Calculation of Compressible Turbulence Boundary Layers with Heat and Mass Transfer. AIAA Paper 70-0741, 1970.

12. Johnson, D. A.; and King, L. S.: A Mathematically Simple Turbulence Closure Model for Attached and Separated Turbulent Boundary Layers. AIAA Paper 84-0175, 1984.

13. Abid, R.: Extension of Johnson-King Turbulence Model to 3-D Flows. AIAA Paper 88-0223, 1988.

14. Abid, R.; Vatsa, V. N.; Johnson, D.; and Wedan, B. W.: Prediction of Separated Transonic Wing Flows With Non-Equilibrium Algebraic Model. AIAA Paper 89-0558, 1988.

15. Goldberg, U. C.: Separated Flow Treatment with a New Turbulence Model. AIAA Journal, Vol. 24, No. 10, 1986.

16. Goldberg, U. C.; and Chakravarthy, S.: Separated Flow Predictions Using Hybrid K-L/Backflow Model. AIAA Paper 89-0566, 1989.

17. Chuech, S. G.; Lai, M. C.; and Faeth, G. M.: Structure of Turbulent Sonic Underexpanded Free Jets. AIAA Paper 88-0700, 1988.

18. Capone, F. J.: Summary of Propulsive-Lift Research in the Langley 16-Foot Transonic Tunnel. J. Aircraft, Vol. 13, No. 10, Oct. 1976, pp. 803-808.

19. Hiley, P. E.; Wallace, H. W.; and Booz, D. E.: Nonaxisymmetric Nozzles Installed in Advanced Fighter Aircraft. J. Aircraft, Vol. 13, No. 12, Dec. 1976.

20. Berrier, B. L.; Palcza, J. L.; and Richard, G. K.: Nonaxisymmetric Nozzle Technology Program - An Overview. AIAA Paper 77-1225, 1977.

38

21. Capone, F. J.: The Nonaxisymmetric Nozzle - It is for Real. AIAA Paper 79-1810, 1979.

22. Stevens, H. L.; Thayer, E. B.; and Fullerton, J. F.: Development of the Multi-Function 2-D/C-D Nozzle. AIAA Paper 81-1491, 1981.

23. Wolf, D. E.; Sinha, N.; and Dash, S. M.: Fully-Coupled Analysis of Jet Mixing Problems: Three-Dimensional PNS Model, SCIP3D. NASA CR-4139, 1988.

24. Anderson, O. L.; and Barber, T. J.: Three Dimensional Analysis of Complex Hot Exhaust Jets. AIAA Paper 88-3705-CP, 1988.

25. Carlson, John R.: Evaluation and Application of VSAERO to a Nonaxisymmetric Afterbody with Thrust Vectoring. SAE Technical Paper, 1987.

26. Swanson, R. C, Jr.: Numerical Solutions of the Navier-Stokes Equations for Transonic Afterbody Flows. NASA TP-1784, 1980.

27. Swanson, R. C.: Navier-Stokes Solutions for Nonaxisymmetric Nozzle Flows. AIAA Paper 81-1217, 1981.

28. Deiwert, G. S.: Supersonic Axisymmetric Flow Over Boattails Containing a Centered Propulsive Jet. AIAA Journal, Vol. 22, 1984, pp. 1358,-1365.

29. Deiwert, George S.: Anderson, Alison E.; and Nakahasi, Kazuhiro: Theoretical Analysis of Aircraft Afterbody Flow. Journal of Spacecraft and Rockets, Vol. 24, 1984, pp. 496-503.

30. Deiwert, G. S. and Rothmund, H.: Three-Dimensional Flow Over a Conical Afterbody Containing Centered Propulsive Jet: A Numerical Solution. AIAA Paper 83-1709, 1983.

31. Vatsa, V. N.; Thomas, J. L.; and Wedan, B. W.: Navier-Stokes Computations of Prolate Spheroids at Angle of Attack. AIAA Paper 87-2627-CP, 1987.

32. Compton, William B., III; Thomas, James L.; Abeyounis, William; and Mason, Mary L.: Transonic Navier-Stokes Solutions of Three-Dimensional Afterbody Flows. NASA TM-4111, 1989.

33. Abdol-Hamid, K. S.; and Compton, W. B. III: Supersonic Navier-Stokes Simulations of Turbulent Afterbody Flows. AIAA Paper 89-2194, 1989.

34. Thomas, J. L.; and Newsome, R. W.: Navier-Stokes Computations of Lee-Side Flows Over Delta Wings. AIAA Paper 86-1049, 1986.

35. Anderson, W. K.; Thomas, J. L.; and van Lee, B.: A Comparison of Finite Volume Flux Vector Splittings for Euler Equations. AIAA Paper 85-0122, 1985.

36. van Leer, B.; Thomas, J. L.; Roe, P. L.; and Newsome, R. W.: A Comparison of Numerical Flux Formulas for the Euler and Navier-Stokes Equations. AIAA paper 87-1104-CP, 1987.

37. Vigneron, Y. C.; Rakich, J. V.; and Tannehill, J. C.: Calculation of Supersonic Viscous Flow over Delta Wings with Sharp Subsonic Leading Edges. AIAA Paper 78-1378, 1987.

38. Newsome, R. W.; Walters, R. W.; and Thomas, J. L.: An Efficient Iteration Strategy for Upwind/Relation Solutions to the Thin-Layer Navier-Stokes Equations. AIAA Paper 87-1113, 1987.

39. Eiseman, P. R.: Alternate Direction Adaptive Grid Generation. AIAA Journal, vol. 23, pp. 551-560, 1985.

40. Eiseman, P. R.; and Erlebacher, G.: Grid Generation for the Solution of Partial Differential Equations. ICASE Report No. 87-57. NASA CR-178365, 1987.

41. Eiseman, P. R.: Adaptive Grid Generation, Computer Methods in Applied Mechanics and Engineering, vol. 64, pp 321-376, 1987.

42. Love, E. S.; Grigsby, L. P.; Lee, L. P.; and Woodling, M. J.: Experimental and Theoretical Studies of Axisymmetric Free Jets. NASA TR-R6, 1959.

43. Norum, T. D.; and Seiner, J. M.: Measurements of Mean Static Pressure and Far Field Acoustics of Shock-containing Supersonic Jets. NASA TM-84521, 1984.

44. Wlezien, R. W.; and Kibens, V.: Influence of Nozzle Asymmetry on Supersonic Jets. AIAA Journal, vol. 26, no. 1, pp. 27-33, 1988.

40

45. Putnam, Lawrence E.; and Mercer, Charles E.: Pitot-Pressure Measurements in Flow Fields Behind a Rectangular Nozzle with Exhaust Jet for Free-Stream Mach Numbers of 0.00, 0.60, and 1.20. NASA TM-88990, 1986.
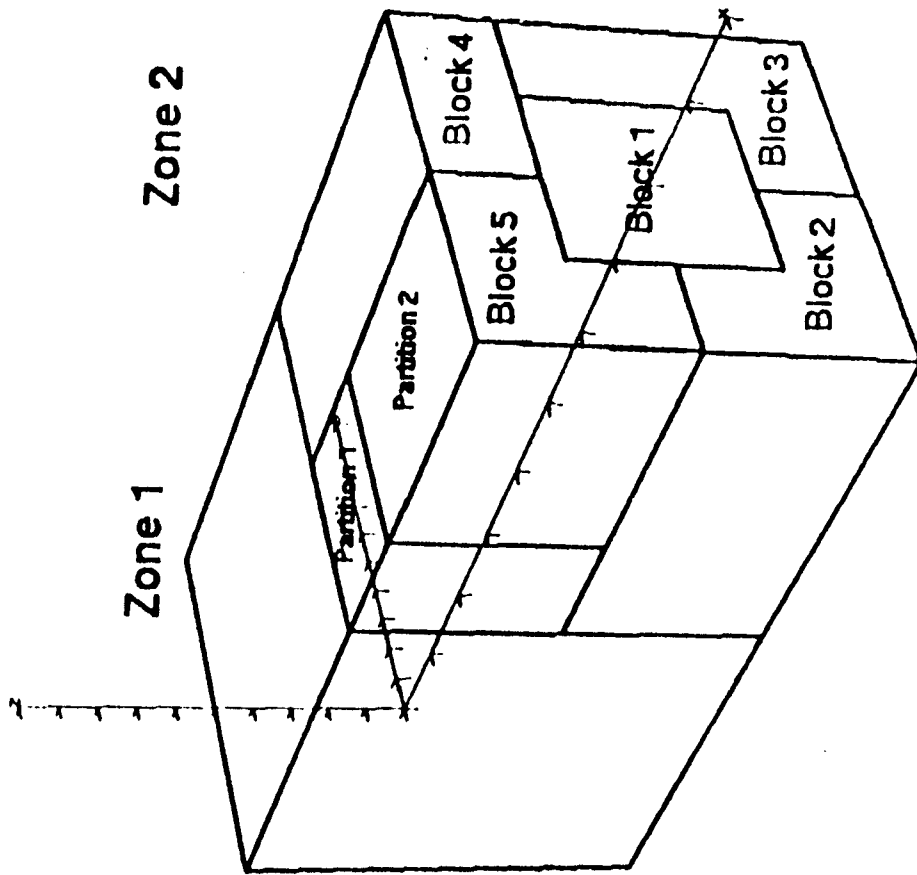
Figure 1. PAB3D-v2 Typical Computational Domain.

Round Nozzle
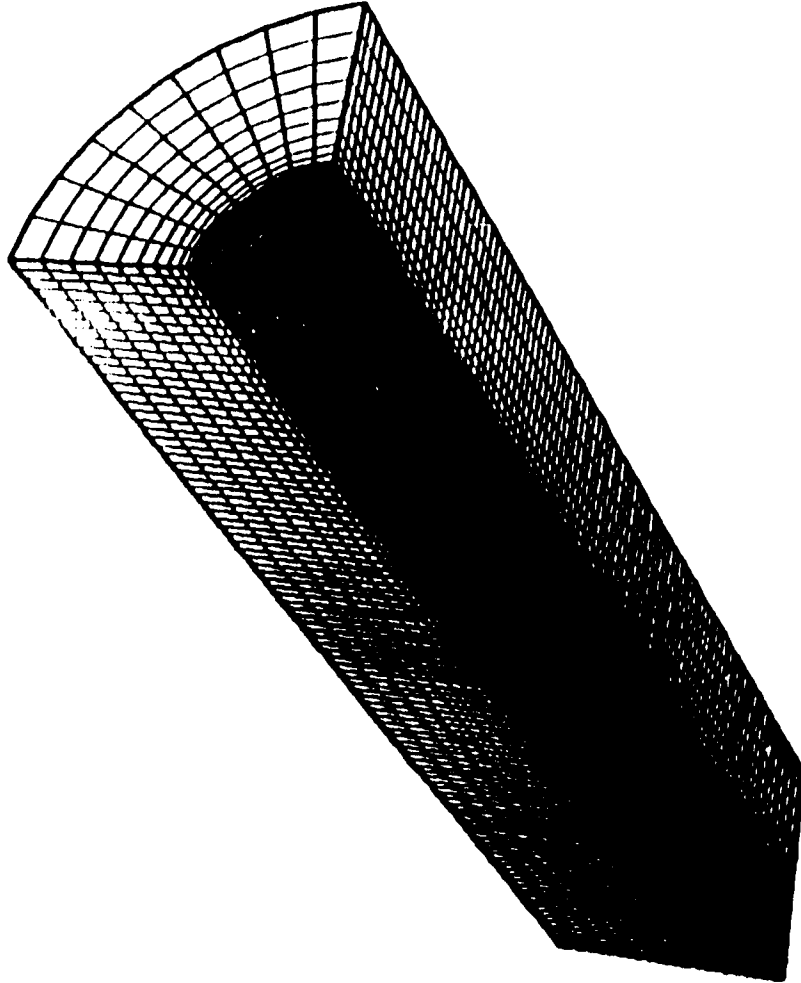
Figure 2. Typical Grid Distribution for the Physical Domain of Axisymmetric Jet.
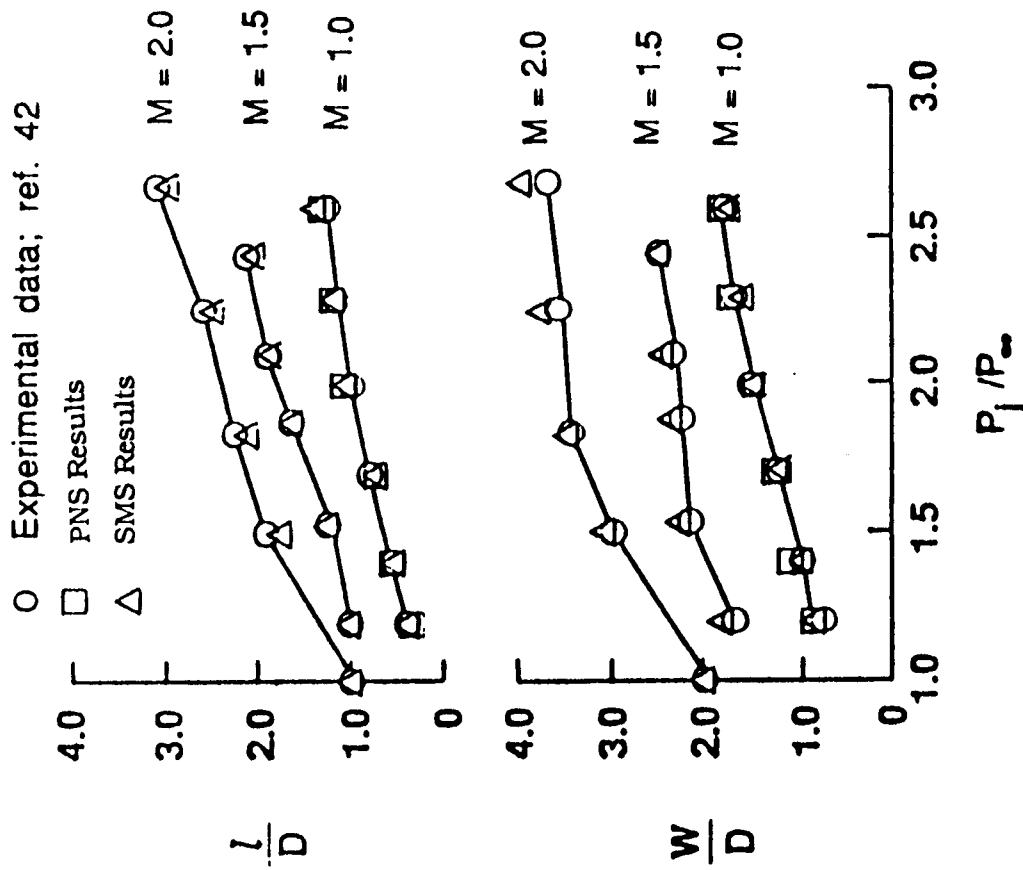
Figure 3. Comparison of Predicted (3D PNS and SMS) and Measured First Shock-Cell Characteristics for Supersonic Free Jets.

44
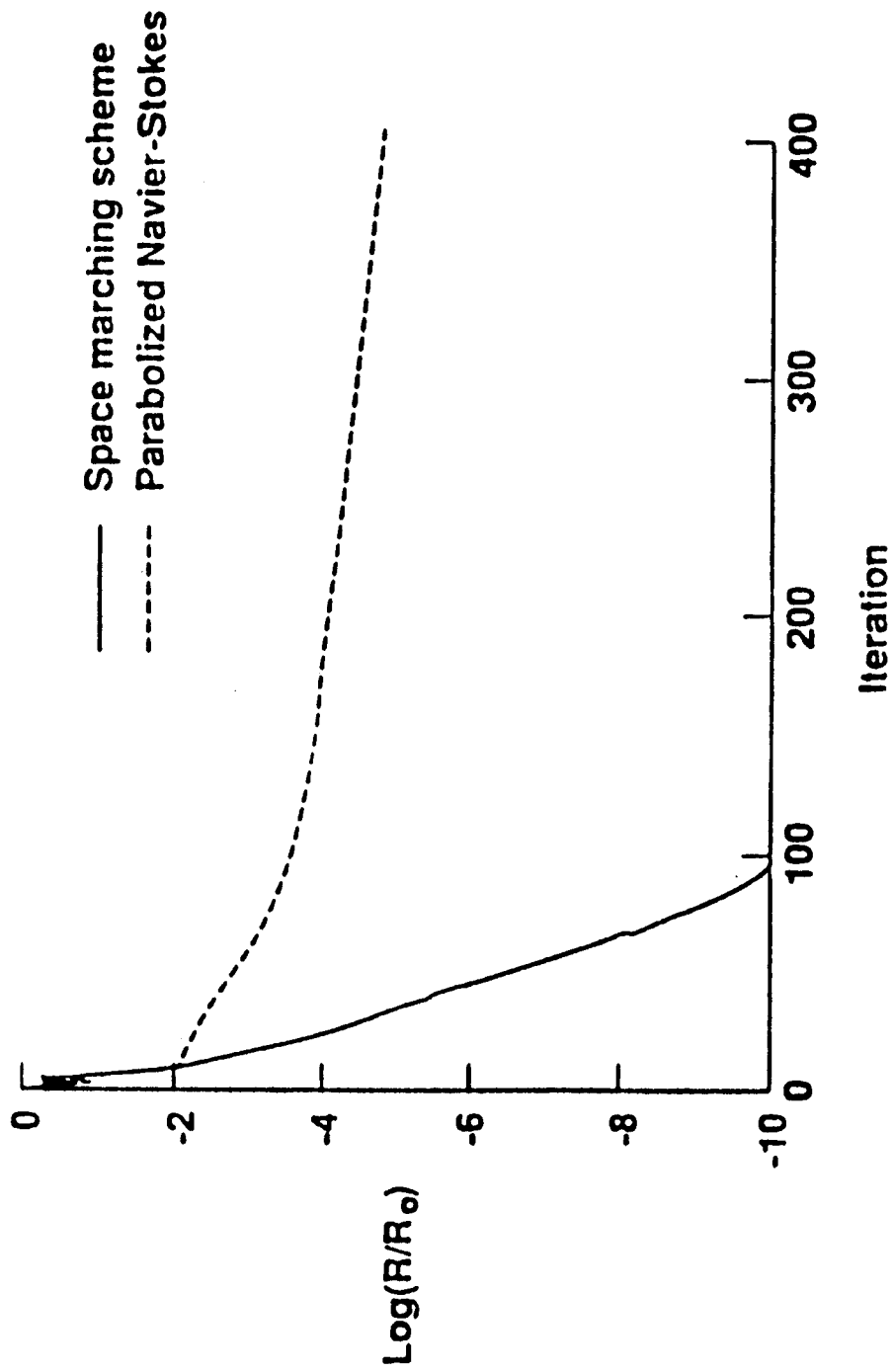
Figure 4. Typical Convergence History for the Space Marching Schemes for M = 2.0 and $P_j/P_a = 1.45$.
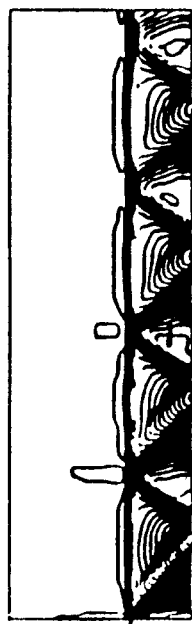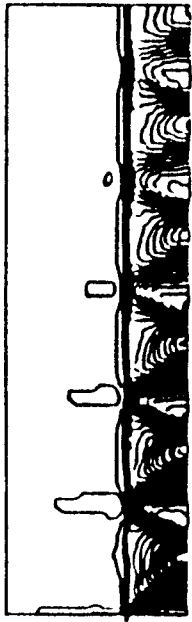
Figure 5. Predicted Mach Contours (3D SMS) for Underexpanded Sonic Jet Operated at different Pressure Ratios.

$P_j/P_a = 1.4$

$P_j/P_a = 2.0$

$P_j/P_a = 1.2$

$P_j/P_a = 1.7$

46
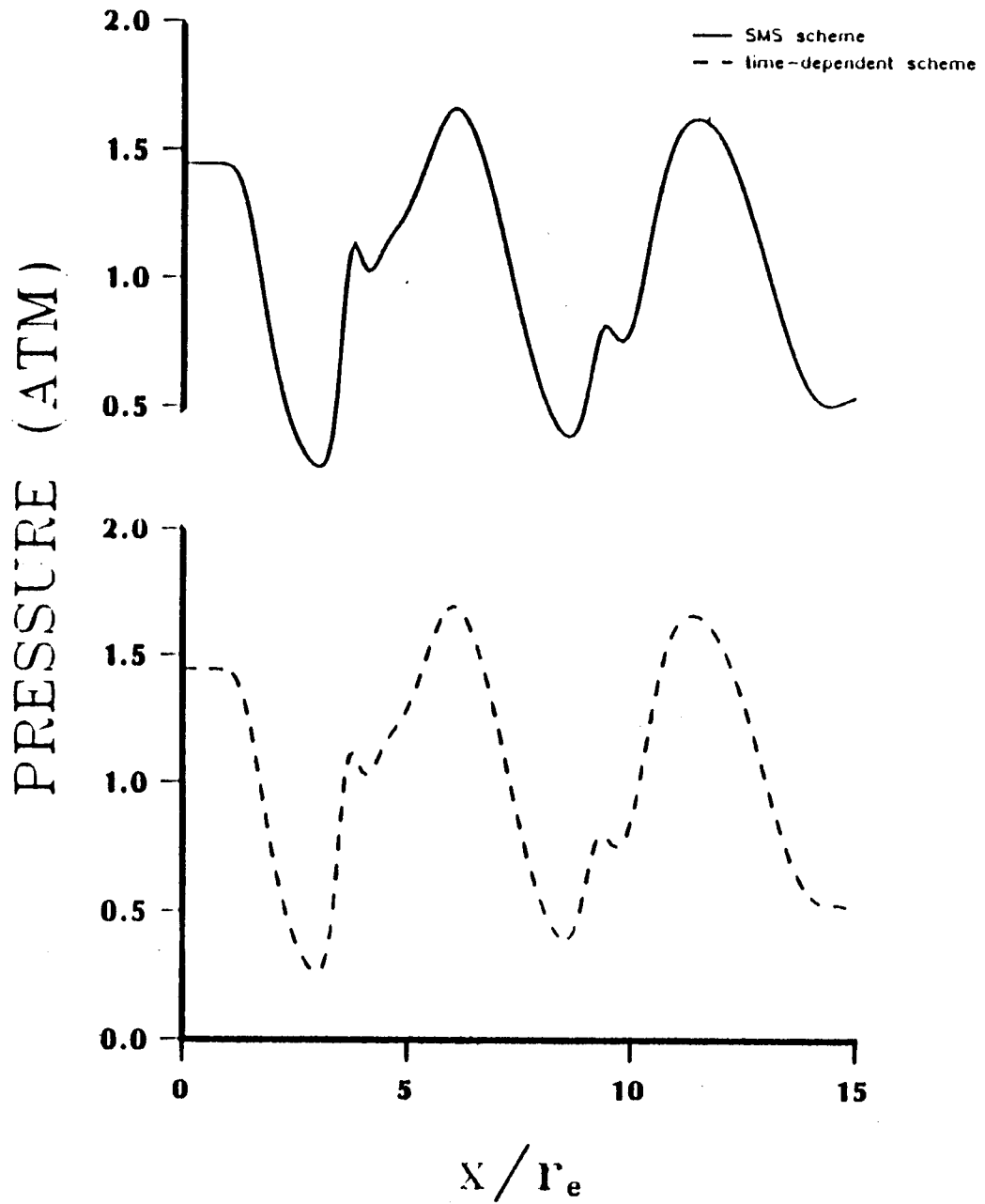
Figure 6. Comparisons Between Time-dependent and Space Marching Solutions in Predicting the Centerline Pressure of Underexpanded Mach 2 Jets and $P_j/P_a = 1.45$.
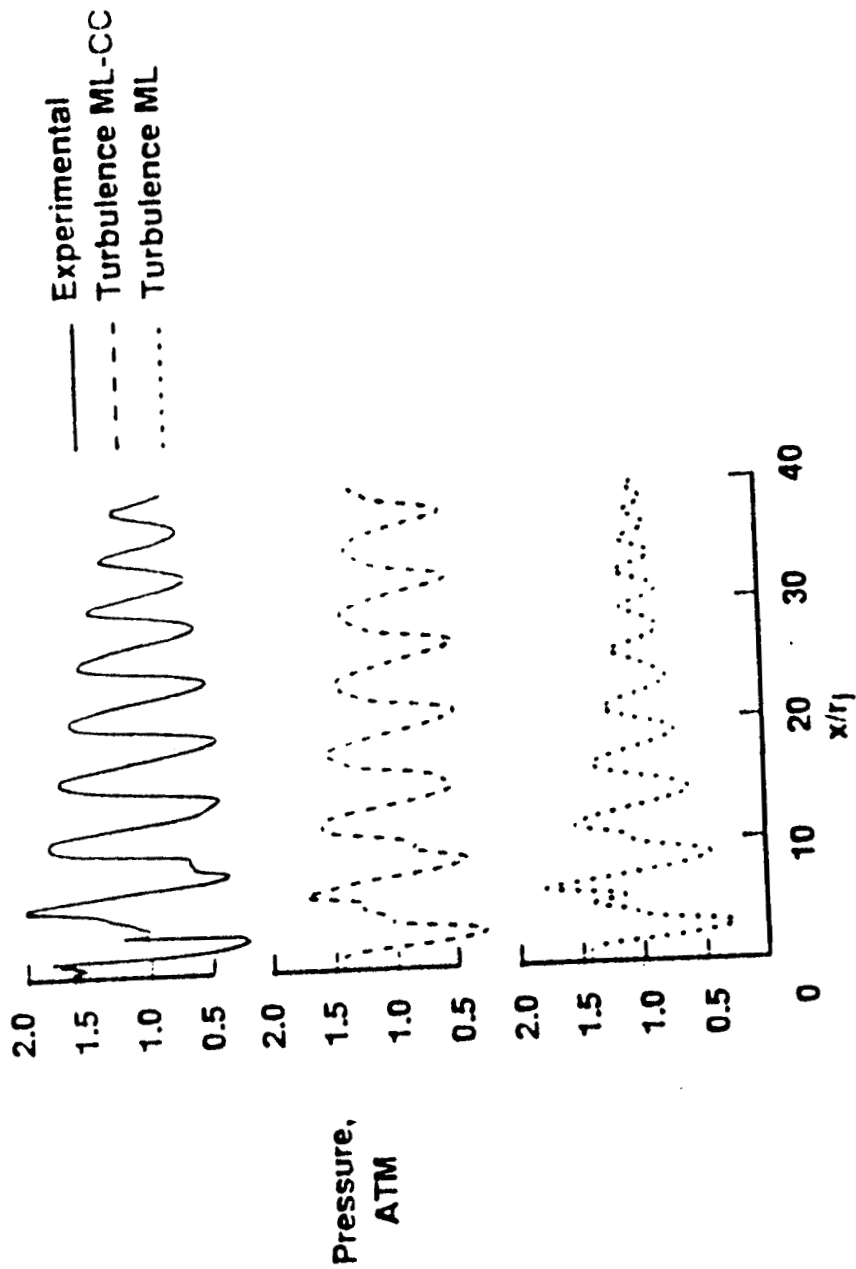
Figure 7. Comparison Between Different Turbulence Models (ML and ML-CC) predictions and measured Centerline Pressure of Underexpanded Mach 2 Jet. $P_j/P_a = 1.45$.

48.
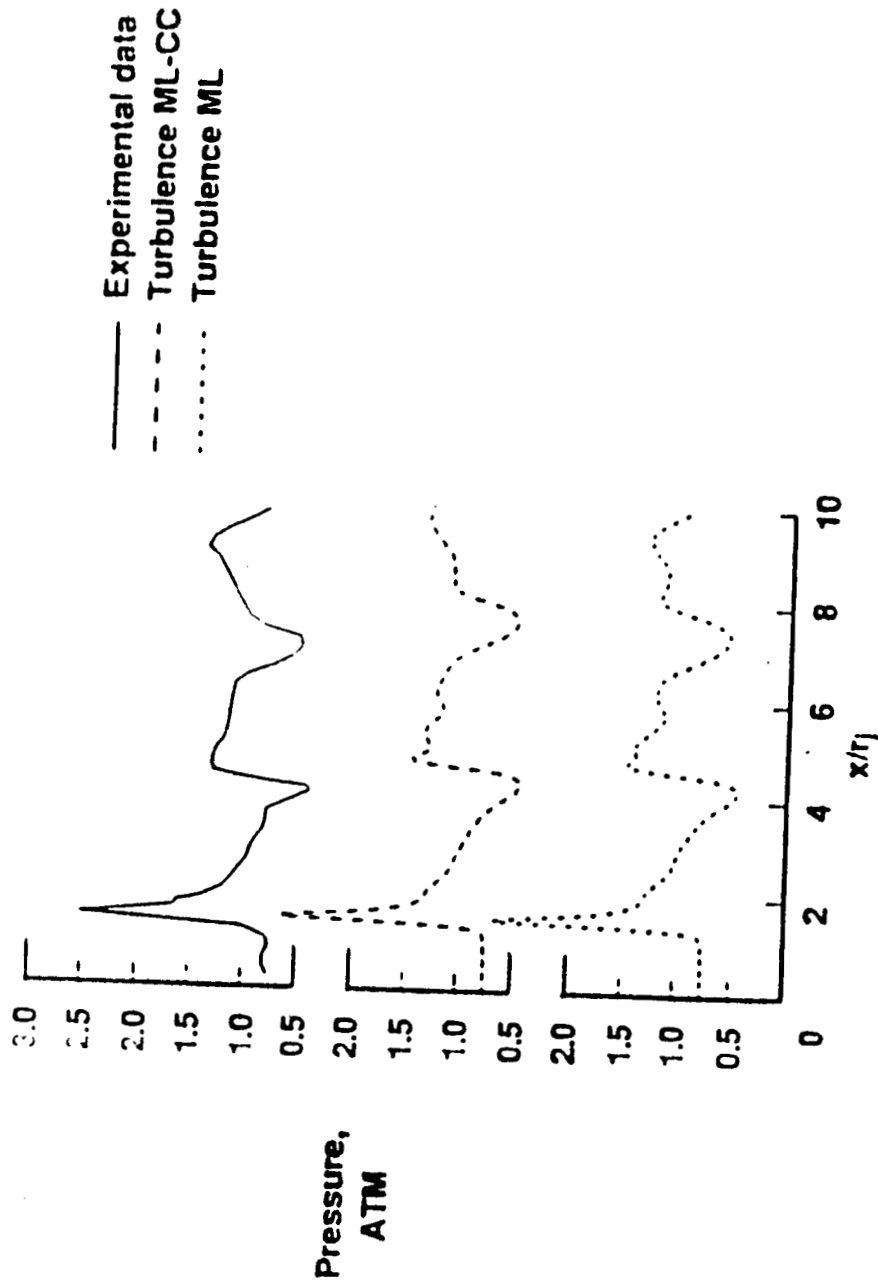
Figure 8. Comparison Between Different Turbulence Models (ML and ML-CC) predictions and Measured Centerline Pressure of Overexpanded Mach 2 Jet. $P_j/P_a = 0.75$.

49
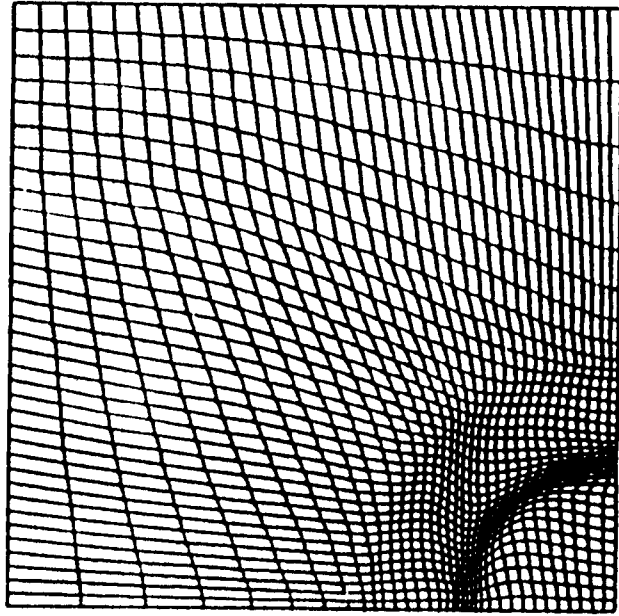
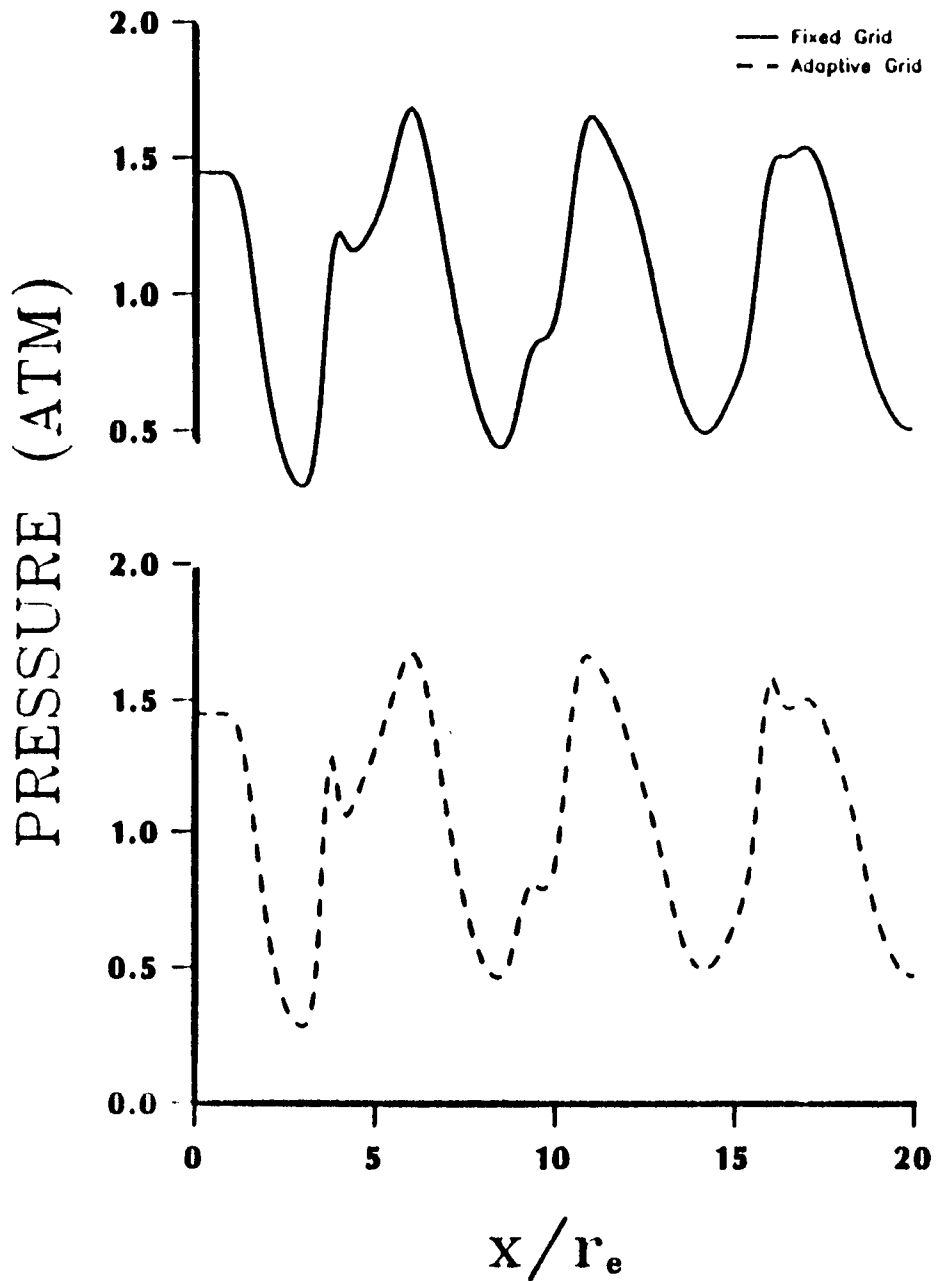Figure 9. Initial Adaptive Grid for a Round Nozzle, Underexpanded Exit Pressure Ratio.
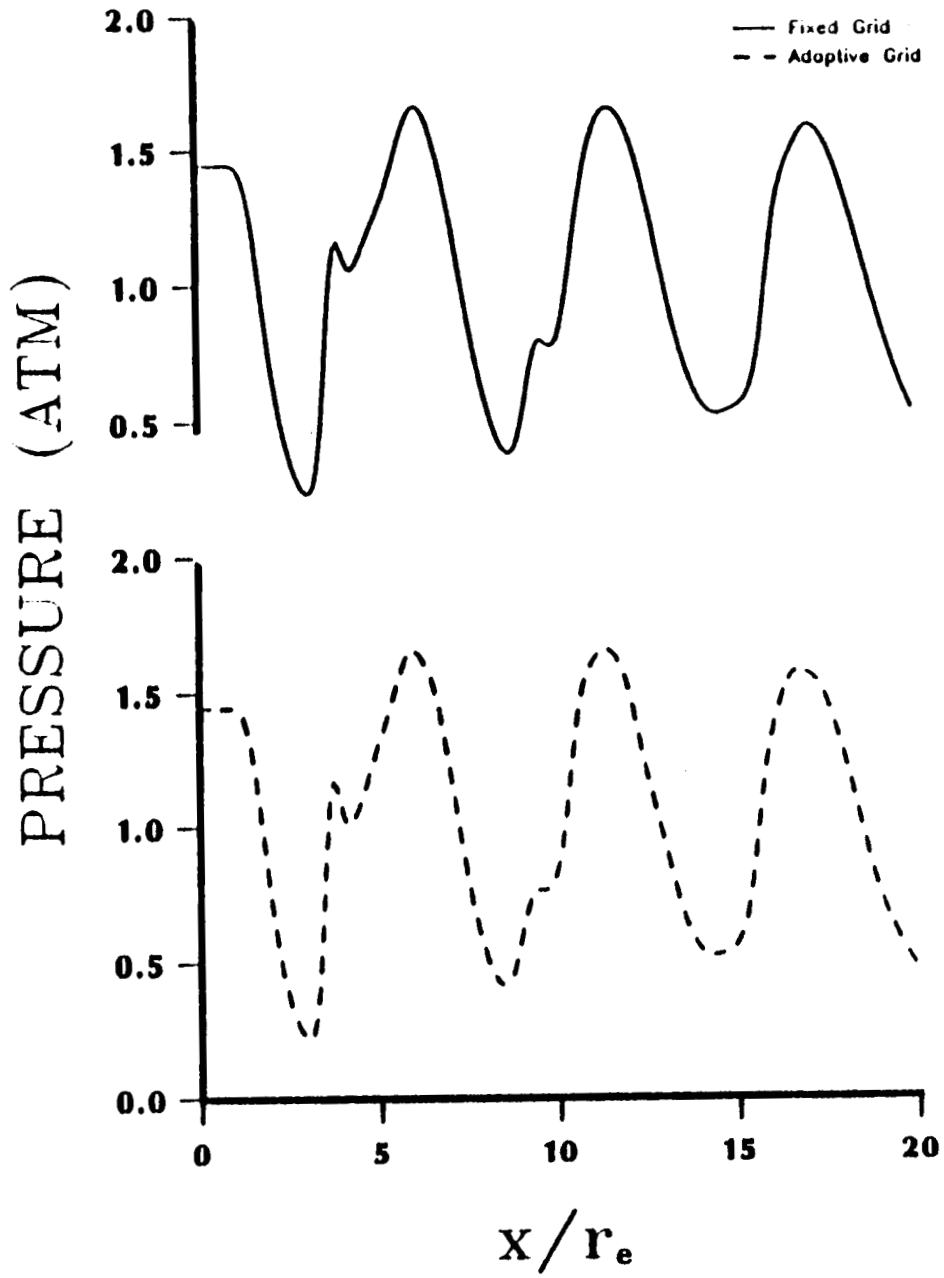
Figure 10. Comparison Between Adaptive and Fixed Grid Calculations in Predicting the Centerline Pressure of Underexpanded Mach 2 Jet.

Round Nozzle
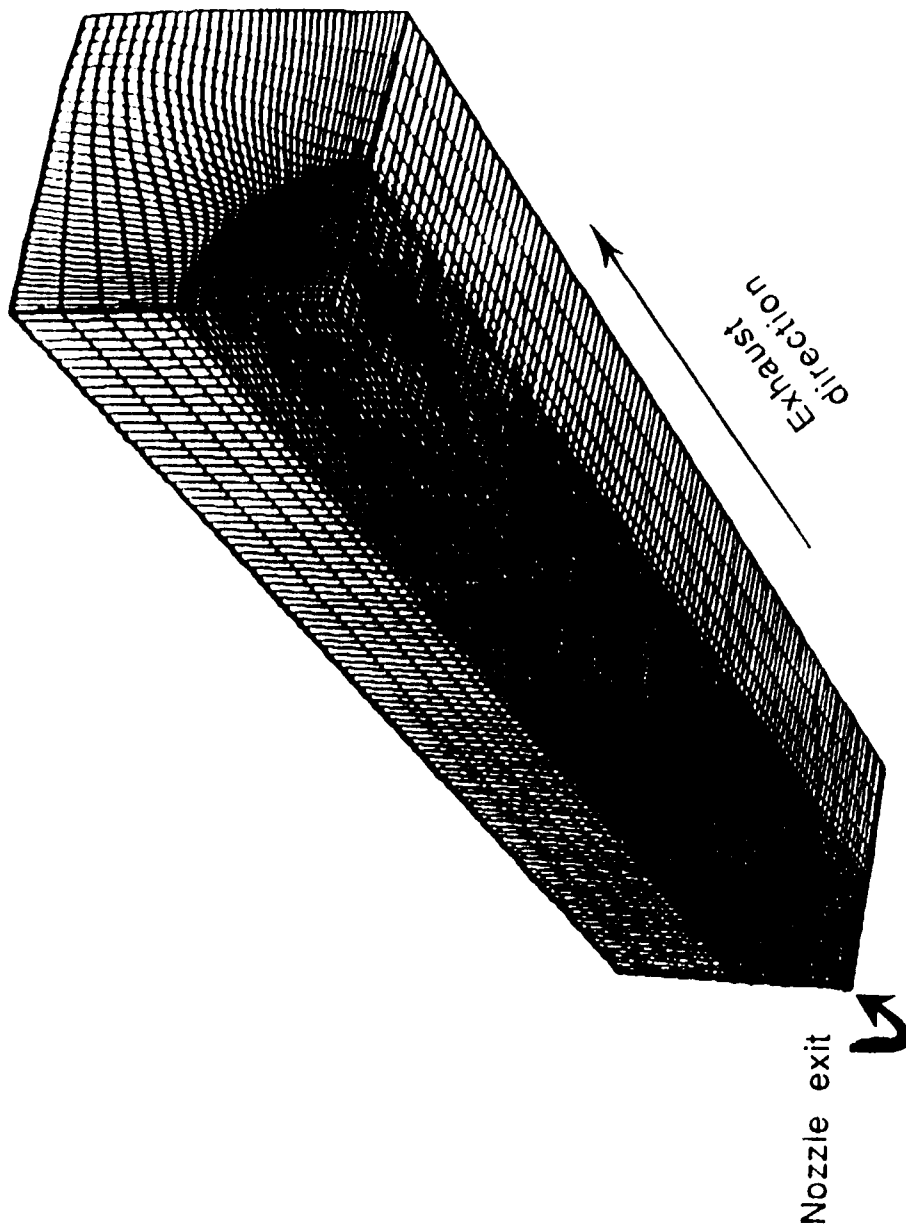
Figure 11. Three-Dimensional Adaptive Grid from Solving Underexpanded Mach 2. round Nozzle Using Single Block Strategy and $P_j/P_a = 1.45$.

52

Round Nozzle

Density

Figure 12. Three-Dimensional Density Contour Predictions for Underexpanded Mach 2 Round Nozzle Using Single Block Strategy. $P_j/P_a = 1.45$.

Exhaust direction

Nozzle exit

Round Nozzle 3-Block Solution
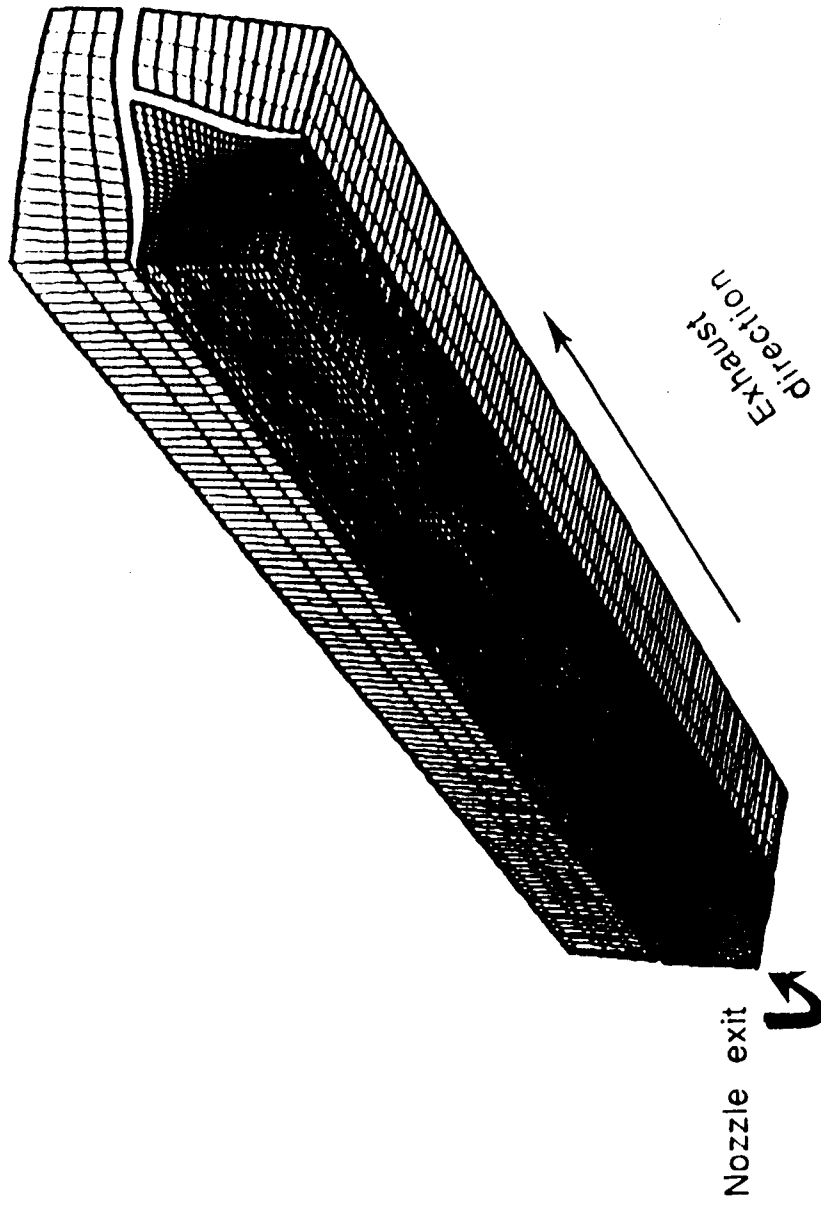
Figure 13. Three-Dimensional Adaptive Grid from Solving Underexpanded Mach 2 Round Nozzle Using Three Block and $P_j/P_a = 1.45$.

5 4

Figure 14. Three-Dimensional Density Contour Predictions for Underexpanded Mach 2 Round Nozzle Using Three Blocks and $P_j/P_a = 1.45$.

5 5
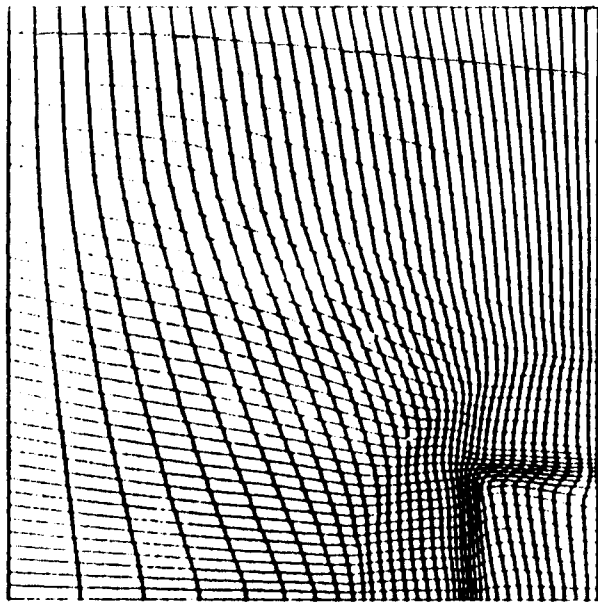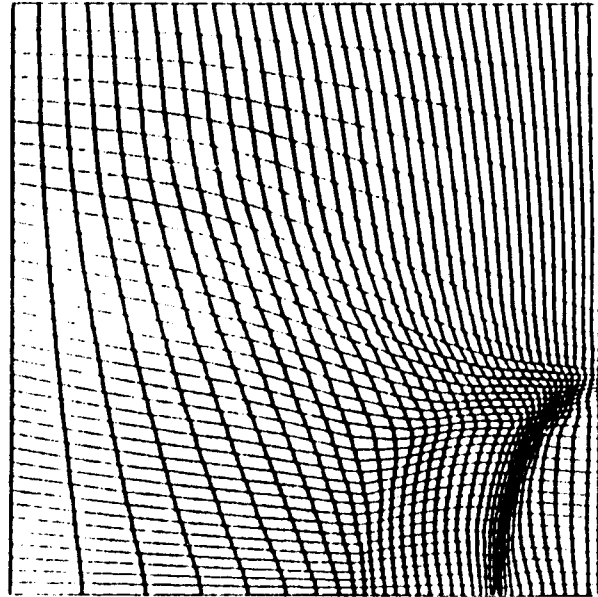
Figure 15. Initial Adaptive Grid for Square and Elliptic Nozzle. Underexpanded Exit Pressure Ratio.

56

Square Nozzle

Density

1.00000
1.10000
1.20000
1.30000
1.40000
1.50000
1.60000
1.70000
1.80000
1.90000
2.00000
2.10000
2.20000
2.30000
2.40000
2.50000
2.60000
2.70000
2.80000
2.90000
3.00000
3.10000
3.20000
3.30000
3.40000
3.50000
3.60000
3.70000

Exhaust
direction

Nozzle exit
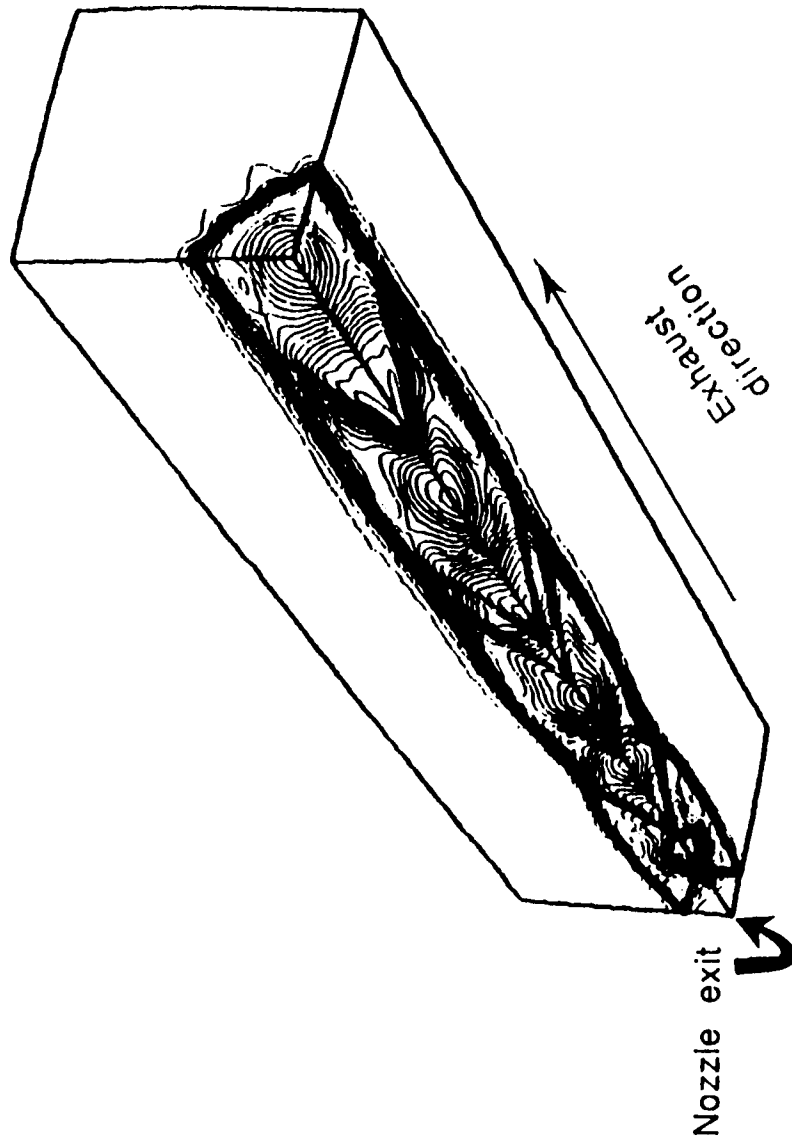
Figure 16. Three-Dimensional Density Contour Predictions for Underexpanded Mach 2 Square Nozzle and $P_j/P_a = 1.45$.

57

Figure 17. Comparison Between Adaptive and Fixed Grid Calculations in Predicting the Centerline Pressure of Underexpanded Mach 2 Square Nozzle and $P_j/P_a = 1.45$

Elliptic Nozzle
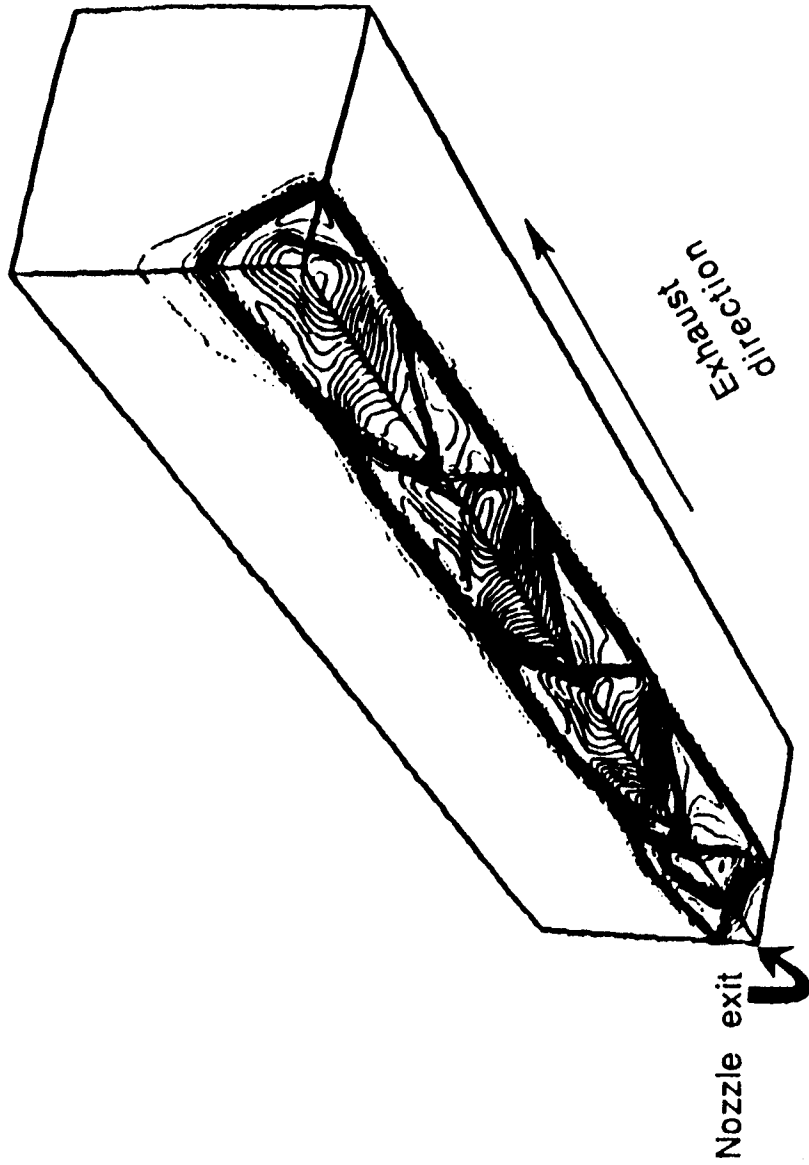
Density

Figure 18. Three-Dimensional Density Contour Predictions for Underexpanded Mach 2 Elliptic Nozzle and $P_j/P_a = 1.45$.

59
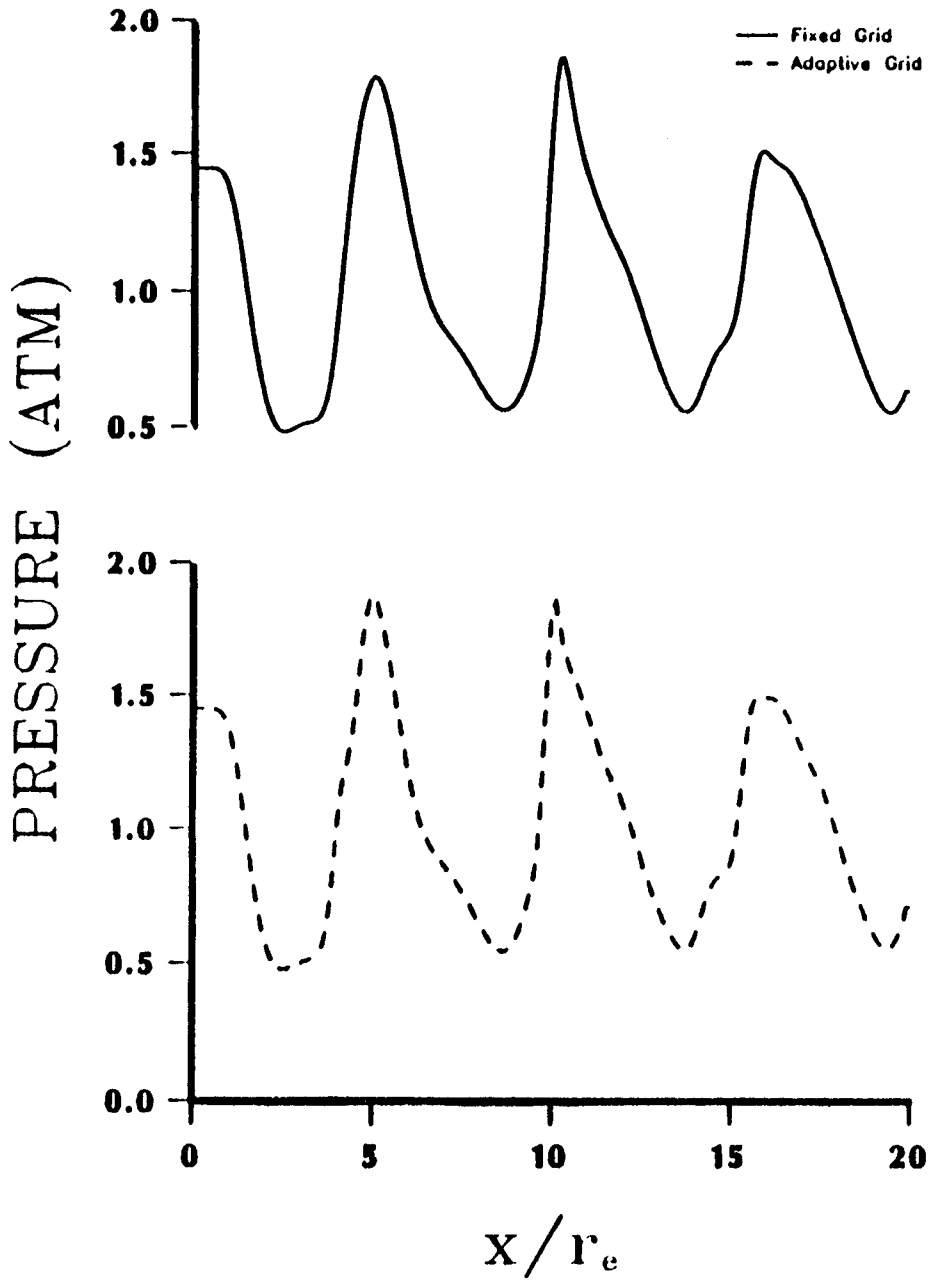
Figure 19. Comparison Between Adaptive and Fixed Grid Calculations in Predicting the Centerline Pressure of Underexpanded Mach 2 Elliptic Nozzle and $P_j/P_a = 1.45$.
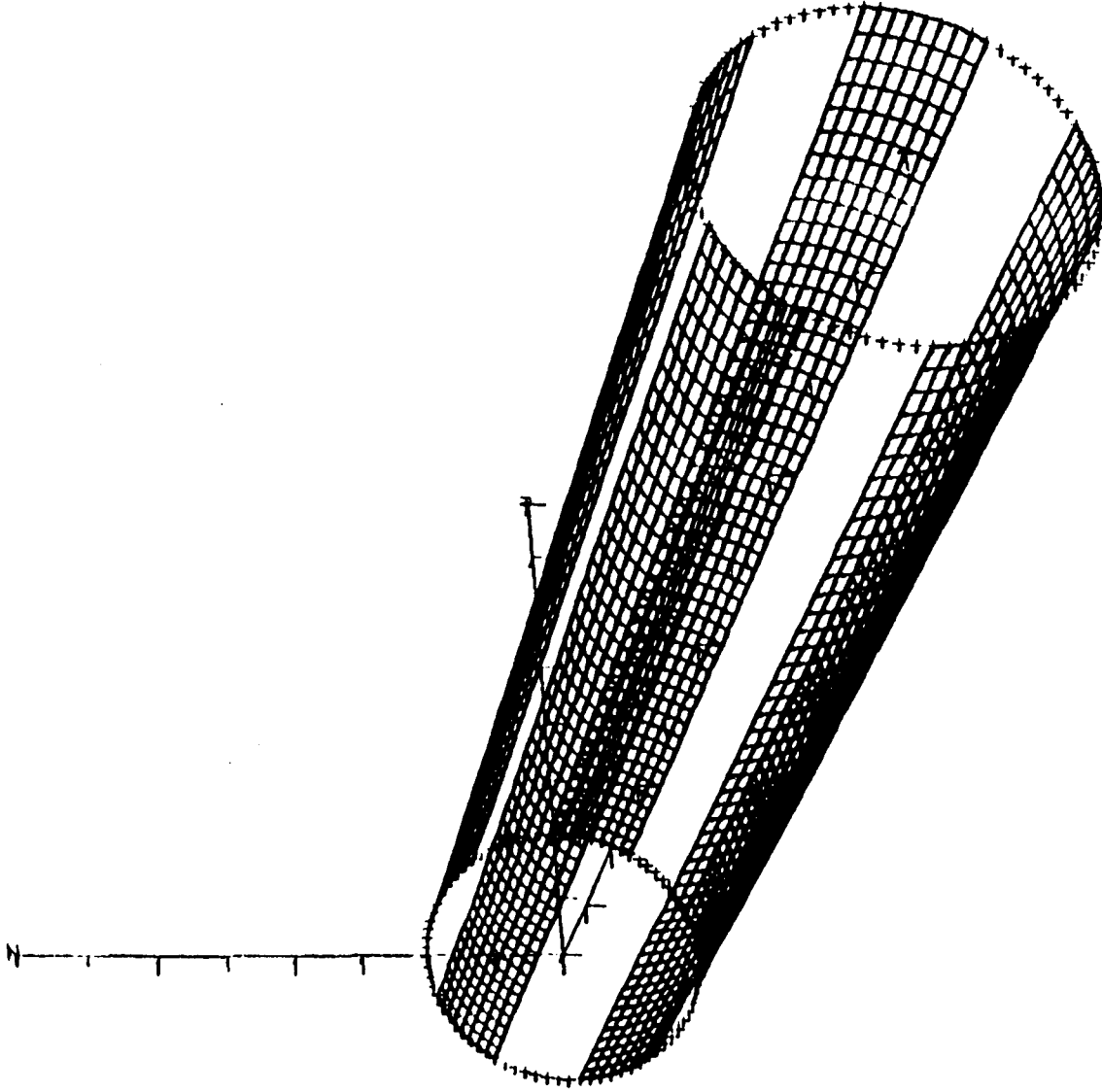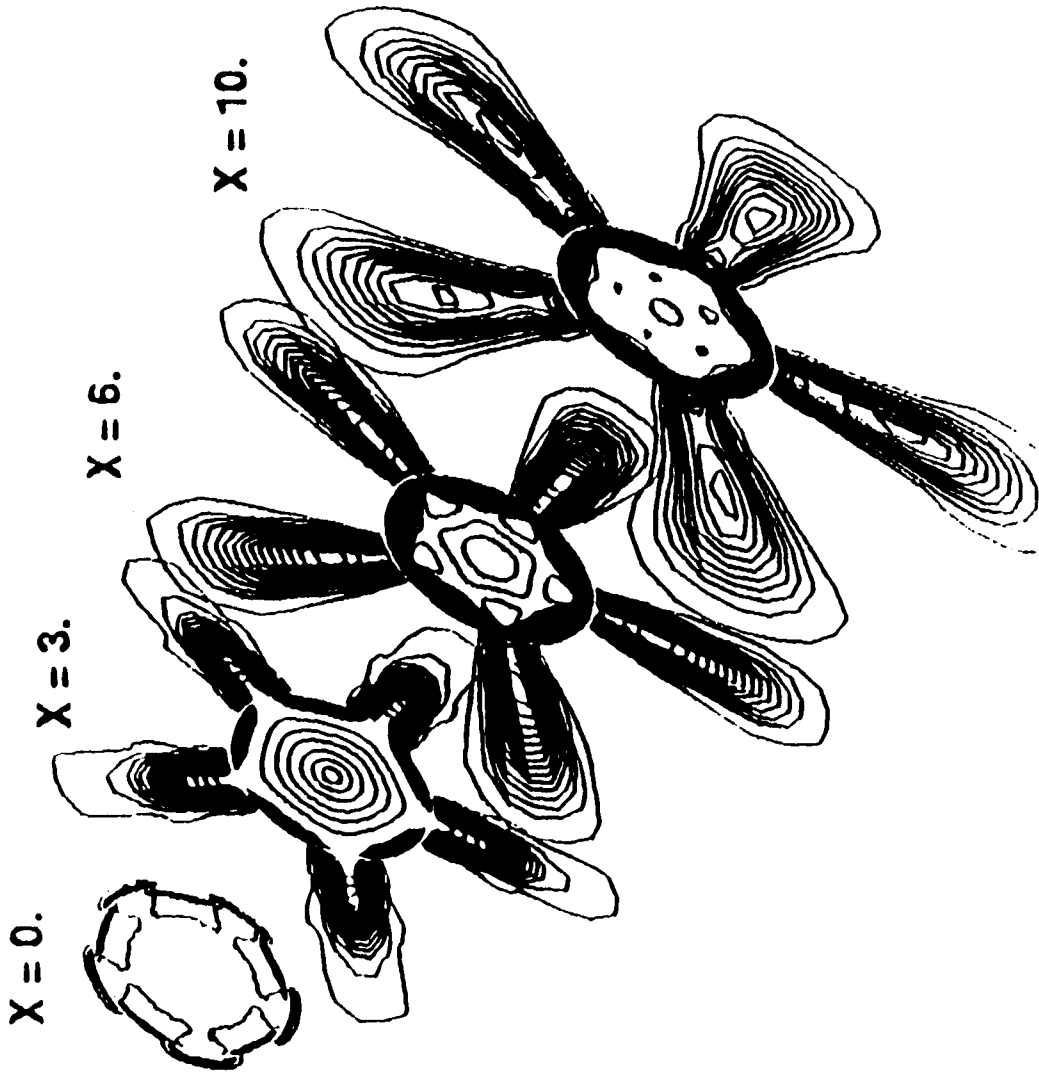
Figure 20. Infinite Tab Nozzle Test Case Configuration.

61
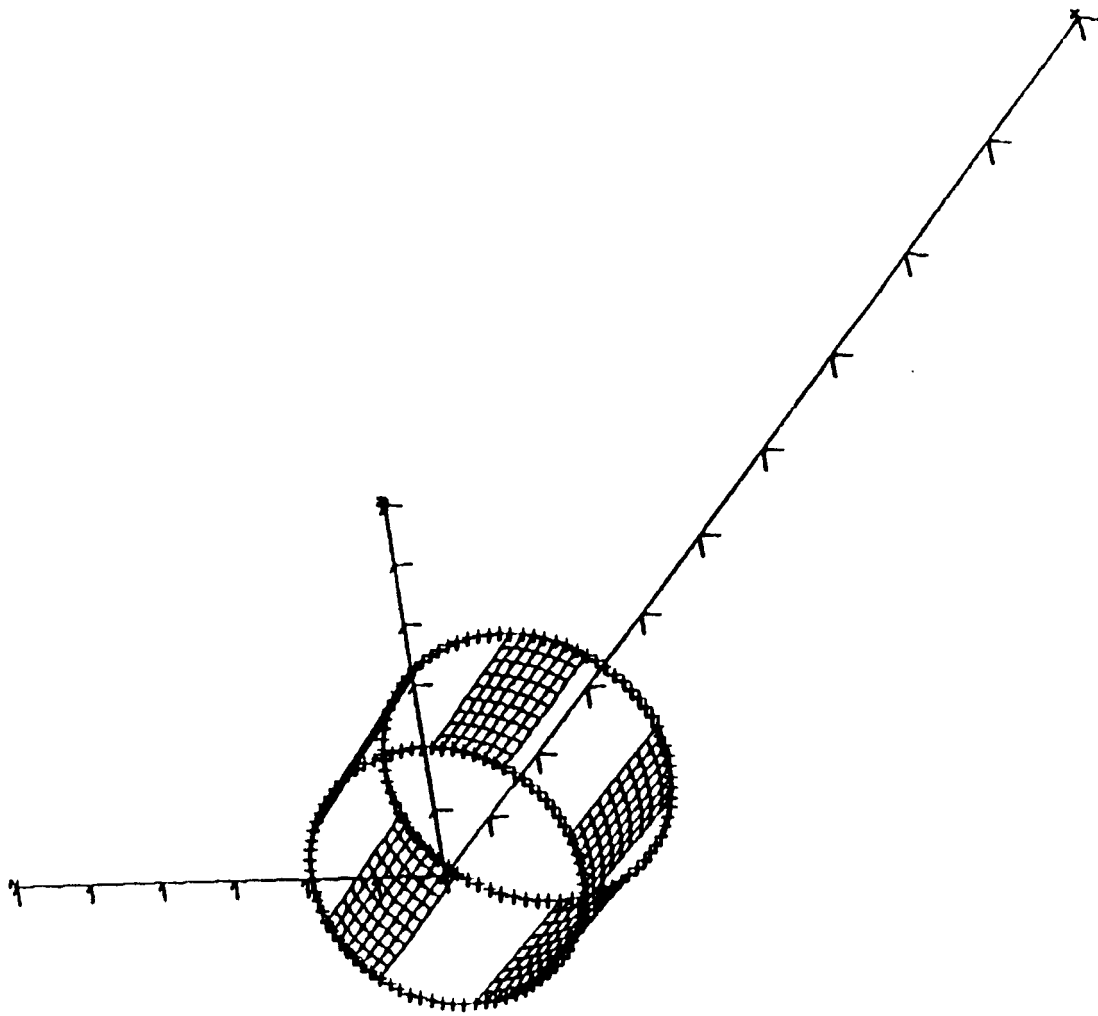
Figure 21. Short Tab Nozzle Jet Test Case Configuration.

62
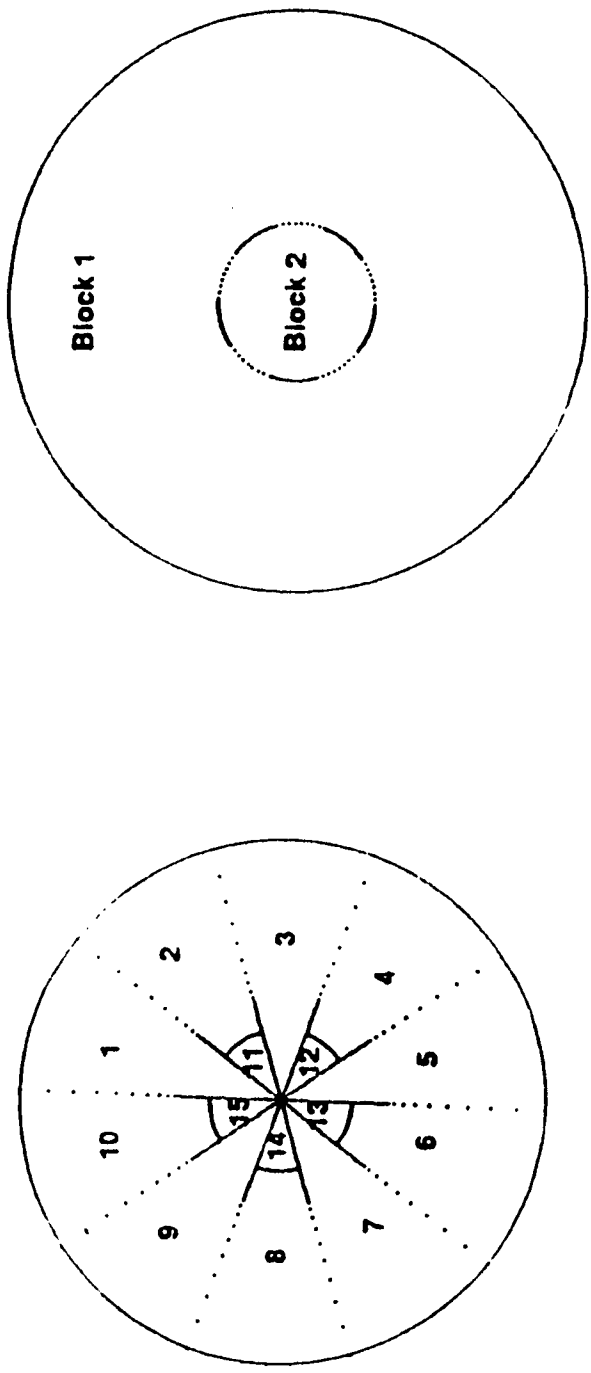
Block 1

Block 2

b) PAB3D-v2 Code

a) CFD Codes

Figure 22. Number of Blocks Required to Solve the 5-Tabs Test Cases.

63

Mach Number

L.0000:
L.1000:
0.20000
0.30000
0.40000
0.50000
0.60000
0.70000
0.80000
0.90000
1.00000
1.10000
1.20000
1.30000
1.40000
1.50000
1.60000
1.70000
1.80000
1.90000
2.00000
2.10000
2.20000
2.30000
2.40000
2.50000
2.60000
2.70000
2.80000
2.90000

X = 0.

X = 3.

X = 6.

X = 10.

Figure 23. Mach Contour Prediction for the Infinite Tab Nozzle at Different Axial Locations.

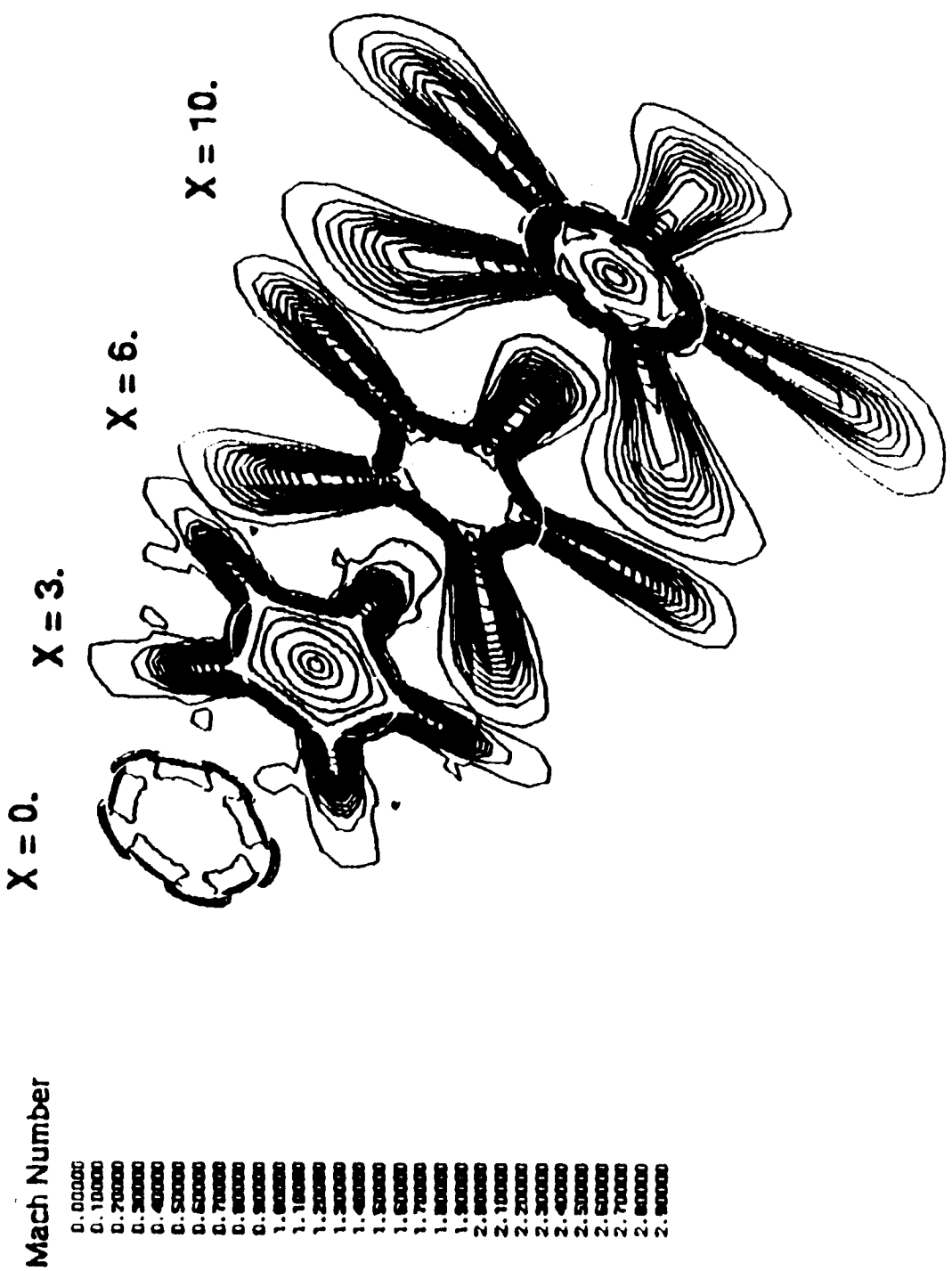Mach Number

X = 0.   X = 3.

X = 6.

X = 10.

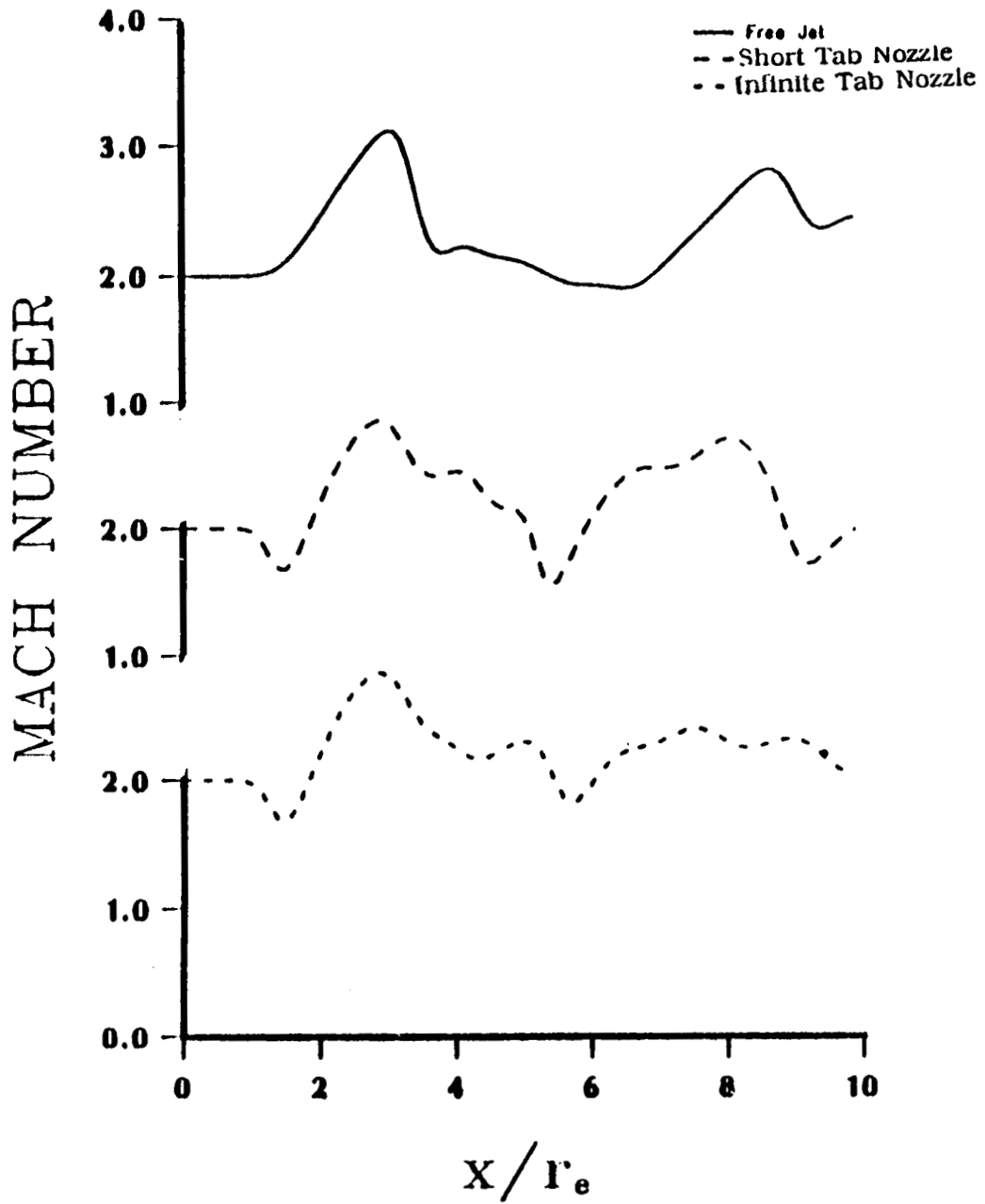Figure 24.   Mach Contour Prediction for the Short Tab Nozzle at Different Axial Locations.

65

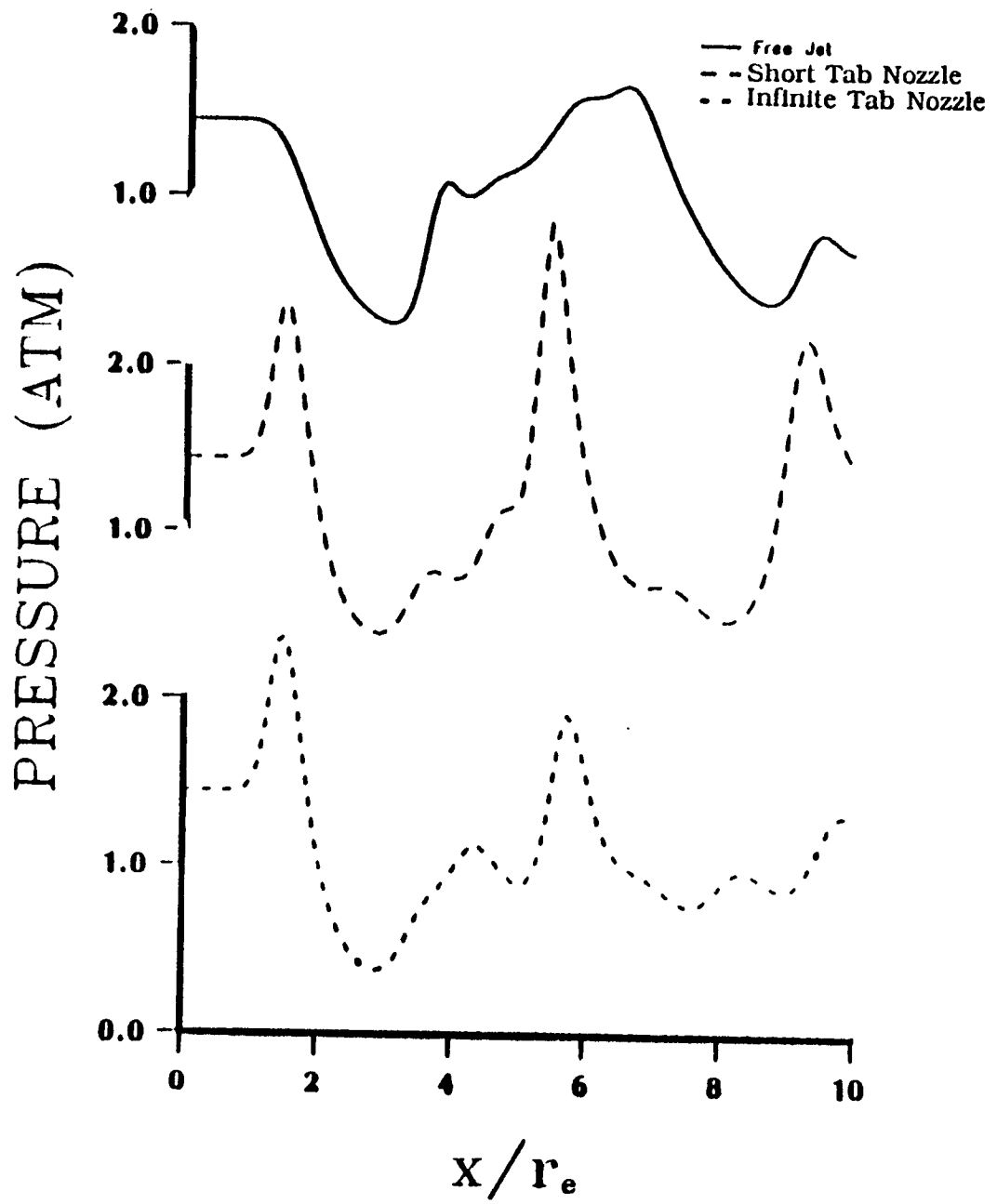Figure 25. Centerline Mach Number Comparisons Between Free-Jet, Infinite and Short Tab Nozzle Solutions.

Figure 26. Centerline Pressure Comparisons Between Free-Jet, Infinite and Short Tab Nozzle Solutions.
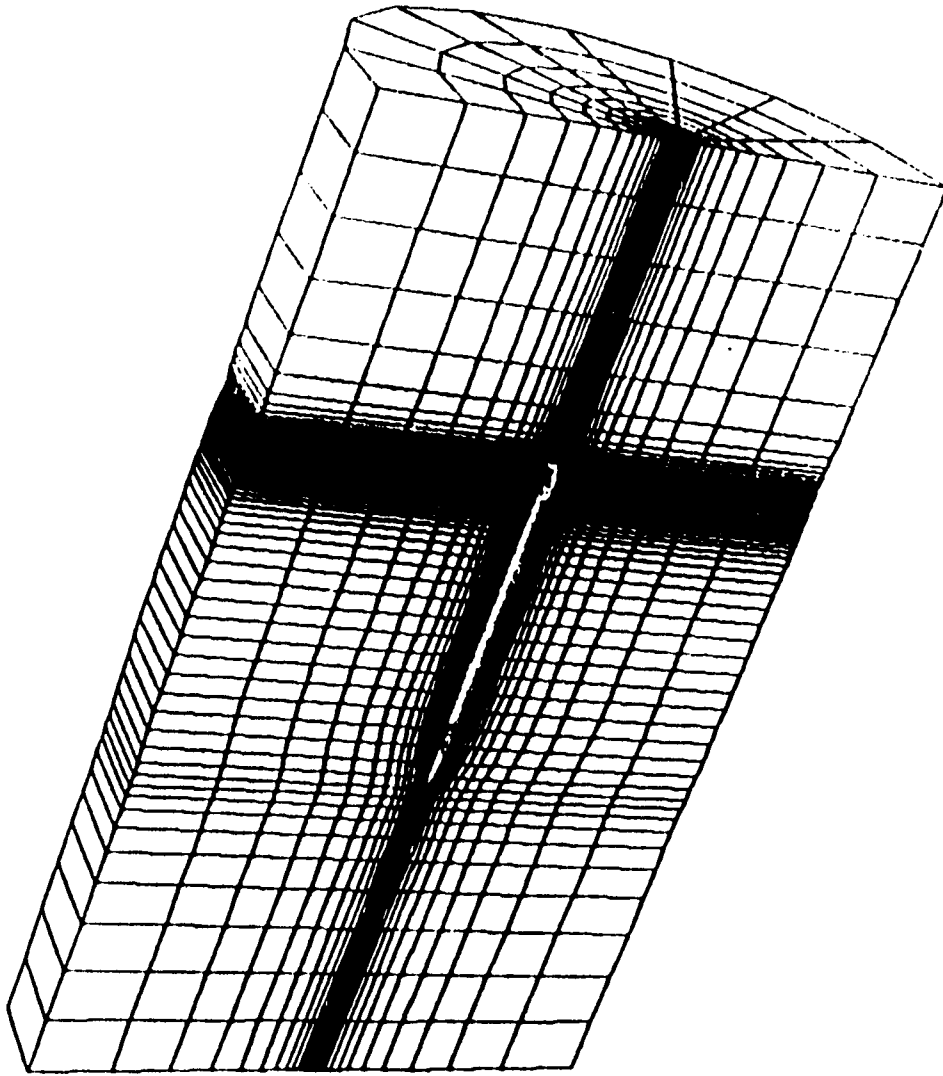
Figure 27. Three-Dimensional Computational Grid for Nonaxisymmetric Afterbody Test Case.

Density

. ((.000)
0. 04000
0. 70000
0. 72000
0. 74000
0. 76000
0. 78000
0. 80000
0. 82000
0. 84000
0. 86000
0. 88000
0. 90000
0. 92000
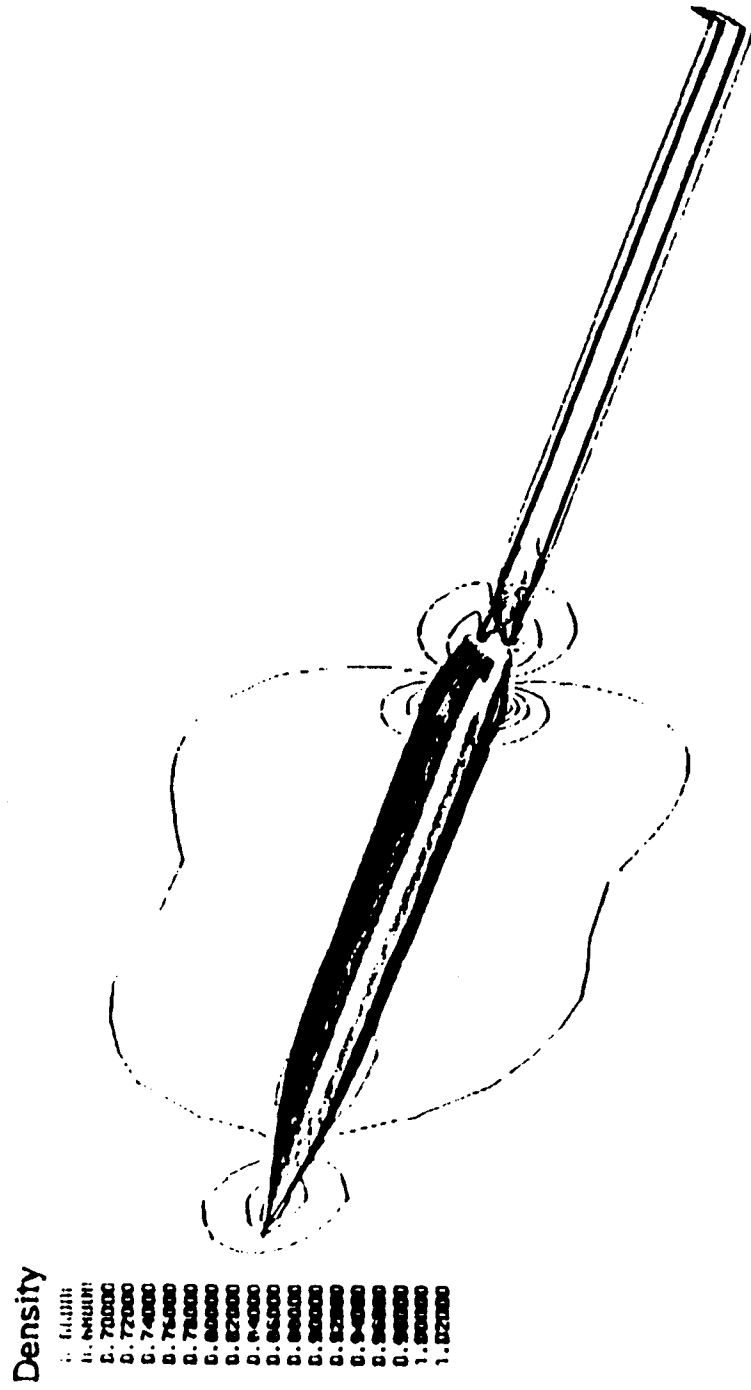0. 94000
0. 96000
0. 98000
1. 00000
1. 02000

Figure 28. Density Contours Prediction for Mach 0.8 Case Using 1Z-2B Topology.
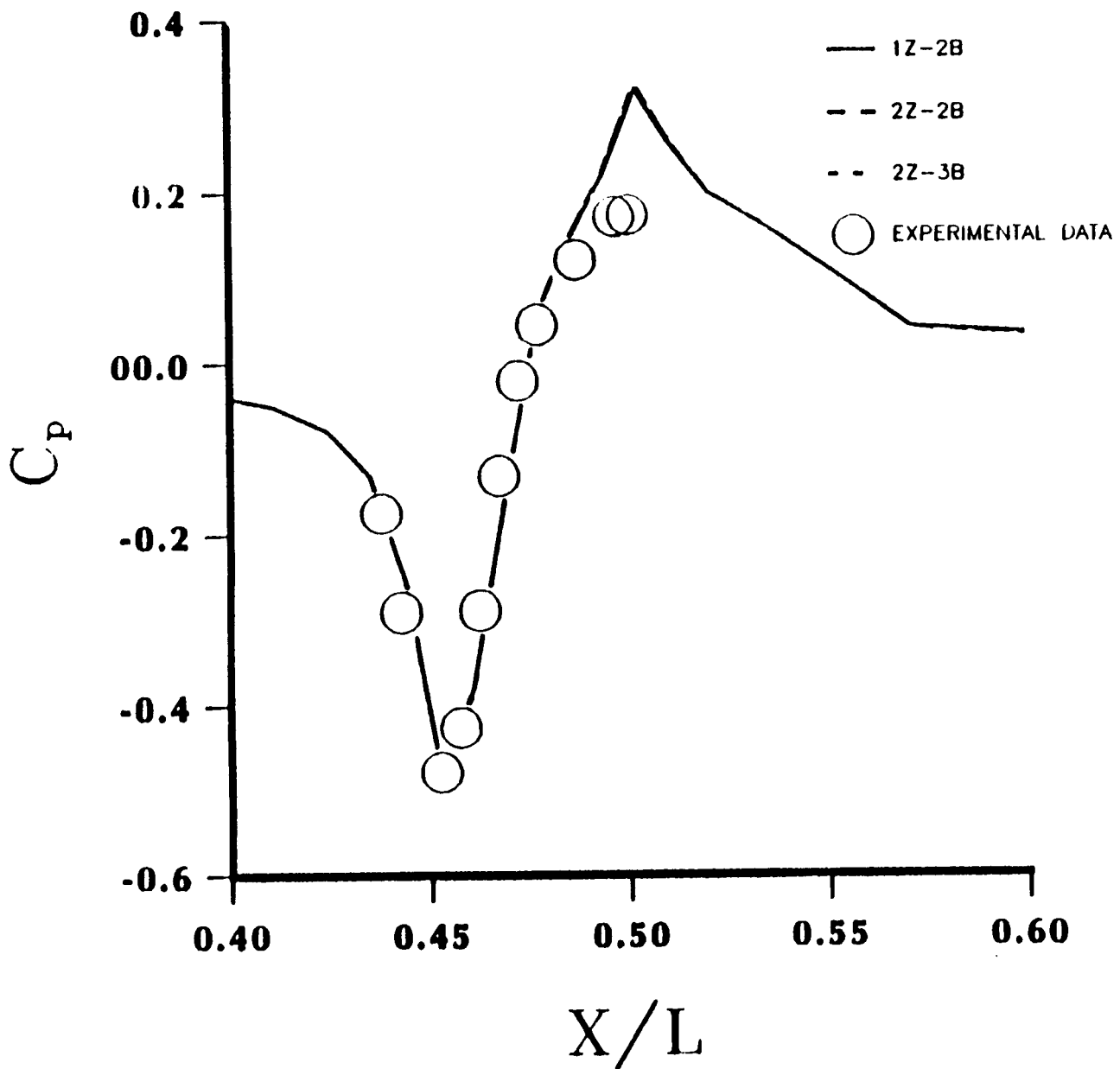
Figure 29. Comparisons Between the Predictions of the Three Different Multiblock/Multizone Topologies (1Z-2B, 2Z-2B and 2Z-3B) for Mach 0.8 Test Case.
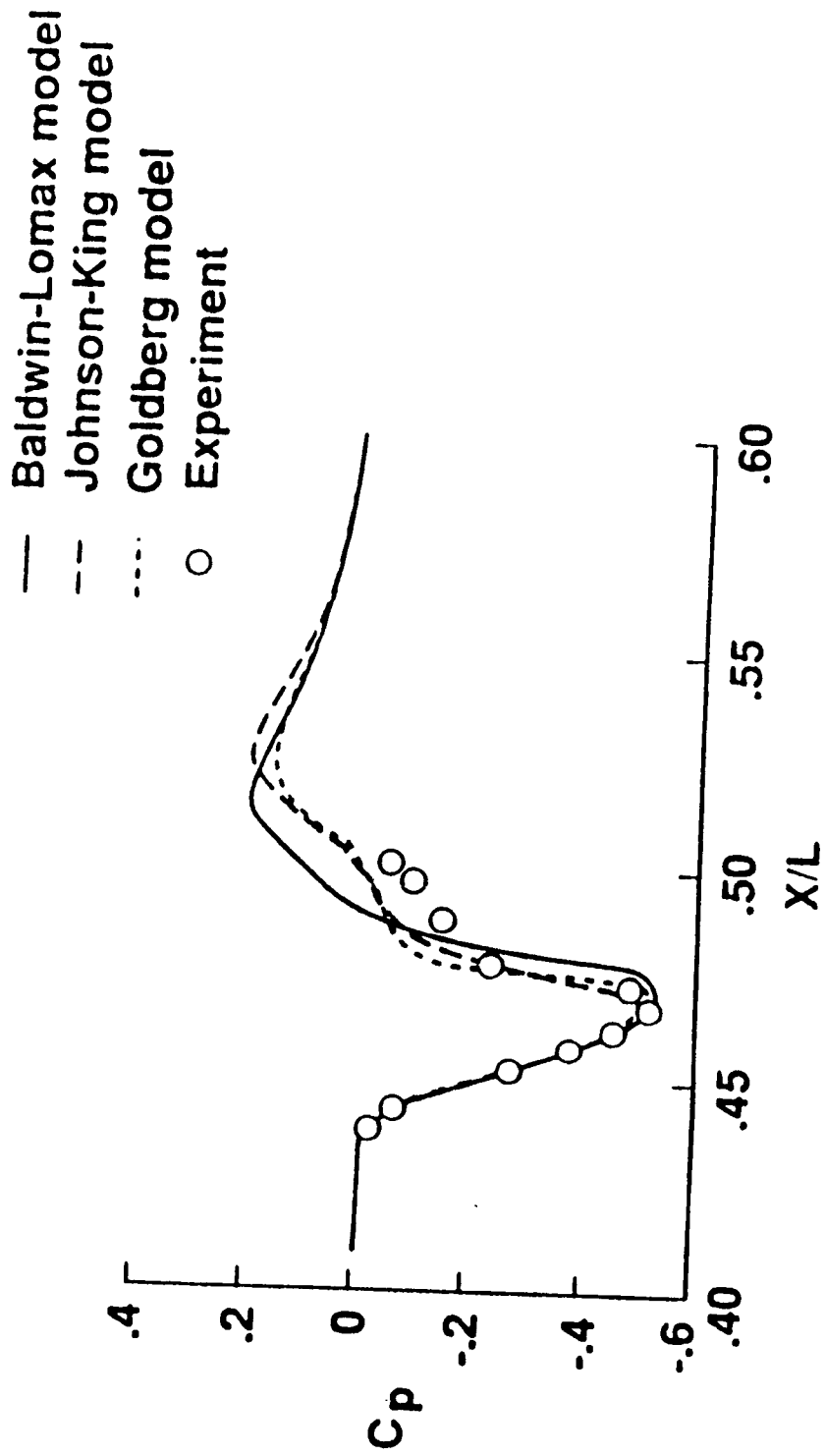
Figure 30. Effect of Turbulence Models (Baldwin-Lomax, Johnson-King and Goldberg) in Predicting C_p for Mach 1.2 Test Case.

NASA
National Aeronautics and Space Administration

Report Documentation Page

1. Report No.	2. Government Accession No.	3. Recipient's Catalog No.
NASA CR-182032		

4. Title and Subtitle	5. Report Date
A Multiblock/Multizone Code (PAB 3D-v2) for the Three-Dimensional Navier-Stokes Equations: Preliminary Applications	September 1990
	6. Performing Organization Code

7. Author(s)	8. Performing Organization Report No.
Khaled S. Abdol-Hamid	
	10. Work Unit No.
	505-68-91-06

9. Performing Organization Name and Address	11. Contract or Grant No.
Analytical Services and Materials, Inc. 107 Research Drive Hampton, VA 23666	NAS1-18599
	13. Type of Report and Period Covered

12. Sponsoring Agency Name and Address	
National Aeronautics and Space Administration Langley Research Center Hampton, VA 23665-5225	Contractor Report
	14. Sponsoring Agency Code

15. Supplementary Notes

Langley Technical Monitor: Bobby L. Berrier
Final Report

16. Abstract

This report describes the development and applications of multiblock/multizone and adaptive grid methodologies for solving the three-dimensional simplified Navier-Stokes equations. The program was initiated in 1987 focusing on developing a three-dimensional plume code to simulate the aerodynamic characteristics of a jet, issuing from nonaxisymmetric nozzles. Previously, Abdol-Hamid et. al. introduced the single zone version of the present code (PAB3D-v1) where the parabolized and simplified Navier-Stokes equations were solved. The code was tested and compared with the experimental data for axisymmetric underexpanded and overexpanded supersonic jet flows and transonic flow around a nonaxisymmetric afterbody.

In the present report, adaptive grid and multiblock/multizone approaches are introduced and applied to external and internal flow problems. These new implementations increase the capabilities and flexibility of the PAB3D code in solving flow problems associated with complex geometry.

17. Key Words (Suggested by Author(s))	18. Distribution Statement
Navier-Stokes Multiblock Adaptive Grid Propulsion Aerodynamics Turbulence Models	Unclassified-Unlimited Subject Category 02

19. Security Classif. (of this report)	20. Security Classif. (of this page)	21. No. of pages	22. Price
Unclassified	Unclassified	78	A05

NASA FORM 1626 OCT 86